Article

UVB-Induced Tumor Heterogeneity Diminishes Immune Response in Melanoma

Graphical Abstract

Dissociation of a heterogeneous melanoma cell line into single cell clones (SCCs)

Infer the phylogenetic relationships of the SCCs

Inoculation of SCC mixes generate tumors with defined states of heterogeneity

Intra Tumor Heterogeneity **Mouse model**

Immune response

Intra Tumor Heterogeneity **Patient data**

Patients survival & immune checkpoint response
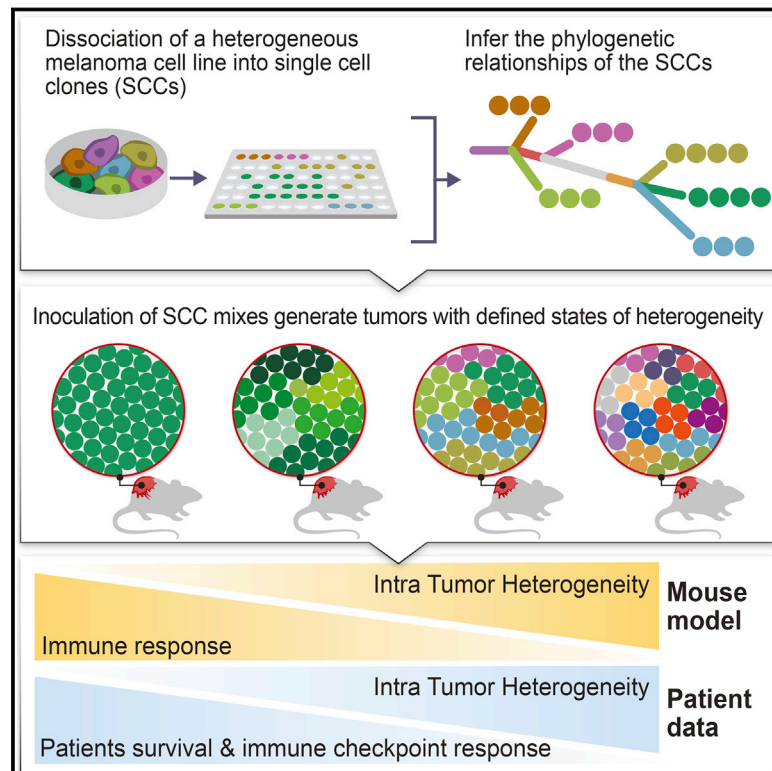
Authors

Yochai Wolf, Osnat Bartok, Sushant Patkar, ..., Charles Swanton, Eytan Ruppin, Yardena Samuels

Correspondence

eyruppin@gmail.com (E.R.), yardena.samuels@weizmann.ac.il (Y.S.)

In Brief

Syngeneic mouse models of melanoma and human patient data are used to explore the effect of intra-tumor heterogeneity on immune response and demonstrate that heterogeneity predicts immunotherapy outcomes better than mutational burden.

Highlights

- Novel mouse system to uncouple tumor mutational load and tumor heterogeneity

- Lower tumor heterogeneity leads to decreased tumor growth because of immune rejection

- Both clone numbers and their genetic diversity mediate tumor growth and rejection

- Tumor heterogeneity is linked to patient survival and checkpoint blockade response

CellPress

UVB-Induced Tumor Heterogeneity Diminishes Immune Response in Melanoma

Yochai Wolf,[1,13] Osnat Bartok,[1,13] Sushant Patkar,[2,14] Gitit Bar Eli,[1,14] Sapir Cohen,[1,14] Kevin Litchfield,[3,11,14] Ronen Levy,[1] Alejandro Jiménez-Sánchez,[4] Sophie Trabish,[1] Joo Sang Lee,[2] Hiren Karathia,[2] Eilon Barnea,[5] Chi-Ping Day,[6] Einat Cinnamon,[7] Ilan Stein,[7] Adam Solomon,[8] Lital Bitton,[1] Eva Pérez-Guijarro,[6] Tania Dubovik,[9] Shai S. Shen-Orr,[9] Martin L. Miller,[4] Glenn Merlino,[6] Yishai Levin,[10] Eli Pikarsky,[7] Lea Eisenbach,[8] Arie Admon,[5] Charles Swanton,[3,11,12] Eytan Ruppin,[2,15,*] and Yardena Samuels[1,15,16,*]

[1]Department of Molecular Cell Biology, Weizmann Institute of Science, Rehovot, Israel
[2]Cancer Data Science Laboratory, Center for Cancer Research, National Cancer Institute, Bethesda, MD, USA
[3]Cancer Evolution and Genome Instability Laboratory, Francis Crick Institute, London NW1 1AT, UK
[4]Cancer Research UK Cambridge Institute, University of Cambridge, Li Ka Shing Centre, Robinson Way, Cambridge CB2 0RE , UK
[5]Faculty of Biology, Technion – Israel Institute of Technology, Haifa, Israel
[6]Laboratory of Cancer Biology and Genetics, Center for Cancer Research, National Cancer Institute, Bethesda, MD, USA
[7]The Lautenberg Center for Immunology and Cancer Research, IMRIC, Hebrew University-Hadassah Medical School, Jerusalem, Israel
[8]Department of Immunology, Weizmann Institute of Science, Rehovot, Israel
[9]Faculty of Medicine, Technion – Israel Institute of Technology, Haifa, Israel
[10]The Nancy and Stephen Grand Israel National Center for Personalized Medicine, Weizmann Institute of Science, Rehovot, Israel
[11]Cancer Research UK Lung Cancer Centre of Excellence London, University College London Cancer Institute, London WC1E 6DD, UK
[12]Department of Medical Oncology, University College London Hospitals, London NW1 2BU, UK
[13]These authors contributed equally
[14]These authors contributed equally
[15]These authors contributed equally
[16]Lead Contact
*Correspondence: eyruppin@gmail.com (E.R.), yardena.samuels@weizmann.ac.il (Y.S.)
https://doi.org/10.1016/j.cell.2019.08.032

SUMMARY

Although clonal neo-antigen burden is associated with improved response to immune therapy, the functional basis for this remains unclear. Here we study this question in a novel controlled mouse melanoma model that enables us to explore the effects of intra-tumor heterogeneity (ITH) on tumor aggressiveness and immunity independent of tumor mutational burden. Induction of UVB-derived mutations yields highly aggressive tumors with decreased anti-tumor activity. However, single-cell-derived tumors with reduced ITH are swiftly rejected. Their rejection is accompanied by increased T cell reactivity and a less suppressive microenvironment. Using phylogenetic analyses and mixing experiments of single-cell clones, we dissect two characteristics of ITH: the number of clones forming the tumor and their clonal diversity. Our analysis of melanoma patient tumor data recapitulates our results in terms of overall survival and response to immune checkpoint therapy. These findings highlight the importance of clonal mutations in robust immune surveillance and the need to quantify patient ITH to determine the response to checkpoint blockade.

INTRODUCTION

It has recently been shown that immunotherapy strategies that enhance the anti-tumor T cell response, such as checkpoint inhibitors and adoptive T cell therapy, have remarkable clinical effects in a wide range of tumor types (Ribas and Wolchok, 2018; Wolf and Samuels, 2018). However, many tumors do not respond to checkpoint inhibitors, and the determinants of treatment efficacy remain largely unknown (Sharma et al., 2017). Neoantigens that arise as a consequence of somatic mutations within the tumor represent an attractive means to promote immune recognition in cancer (Gubin et al., 2014). Indeed, a high tumor mutational burden (TMB) and neoantigen load in tumors have been associated with an enhanced response to immune checkpoint blockade therapy (Chan et al., 2019; Germano et al., 2017; Hellmann et al., 2018; Samstein et al., 2019; Snyder et al., 2014; Van Allen et al., 2015). Cutaneous melanoma, which is among the most highly mutated malignancies (Alexandrov et al., 2013), has the highest objective response rates to checkpoint blockade (~60% upon combined CTLA-4 and PD-1 blockade; Larkin et al., 2015). There is a growing appreciation of the key role of T cells responding to neoantigens in the efficacy of melanoma therapy (Gros et al., 2016; Gubin et al., 2014; Rooney et al., 2015; Strønen et al., 2016). Furthermore, T cell activation and dysfunctional states are essential for controlling tumor immunity (Chihara et al., 2018; Kurtulus et al., 2019; Li et al., 2019; Sade-Feldman et al., 2018).

The leading hypothesis in the immunotherapy field is that tumors with increased TMB present more neoantigens and, thus, are more immunogenic (Germano et al., 2017; Gubin et al., 2015; Hellmann et al., 2018; Rizvi et al., 2015; Strønen et al., 2016; Van Allen et al., 2015). However, tumors containing equally high TMB levels exhibit a variable immune response (Rooney et al., 2015), and some cancers with a low TMB do still respond to immunotherapy (Miao et al., 2018a), which brings into question the association between TMB and immune response. Moreover, the predicted neoantigen load does not correlate with T cell infiltration in melanoma (Spranger et al., 2016), and TMB alone is not a sensitive or specific predictor of treatment outcome (Hugo et al., 2016), suggesting that additional factors determine T cell reactivity.

In parallel, it has recently been reported that intratumor heterogeneity (ITH), manifested by the distribution of clonal versus subclonal mutations and neoantigens (McGranahan and Swanton, 2017; Spranger, 2016), may influence immune surveillance (McDonald et al., 2019; McGranahan et al., 2016; Reuben et al., 2017; Rosenthal et al., 2019). Specifically, clonal neoantigen burden appears to correlate with an improved response to checkpoint inhibitor blockade across a wide range of tumor types (McGranahan et al., 2016; Miao et al., 2018b) and with a favorable outcome following primary non-small-cell lung cancer (NSCLC) surgical resection (Rosenthal et al., 2019). In addition, pan-cancer analyses show better survival for tumors with low ITH (Andor et al., 2016; Jamal-Hanjani et al., 2017; Miao et al., 2018b; Morris et al., 2016). These findings point to ITH as a highly relevant determinant of tumor immune surveillance that merits further experimental evaluation.

Despite past attempts to model the effect of increased TMB (Wang et al., 2017) or ITH (Gejman et al., 2018) on immune response, no efforts have been made to study the combined effects of TMB and ITH in a comparative, causal manner. Here we developed a novel *in vivo* approach to evaluate the contributions of ITH and TMB on immune-mediated tumor rejection and study its parallels in patient data. Using an array of clonal mixing experiments, we further systematically dissect the functional ramifications of the two main components of tumor ITH: the number of clones generating the tumor and their genomic clonal divergence.

RESULTS

ITH Levels Correlate with Melanoma Patient Survival

Neoantigen burden and ITH are associated with overall survival in primary lung adenocarcinomas (McGranahan et al., 2016). Reasoning that these variables may also be associated with melanoma patient survival, we analyzed a cohort of 402 untreated TCGA (The Cancer Genome Atlas; Cancer Genome Atlas Network, 2015) melanoma patients. Patients were grouped based on their mutational load, copy number variation (CNV), and ITH (estimated as the number of clones), which were computed based on each sample's somatic copy number alterations and somatic mutation data (STAR Methods; Figures S1A–S1C). Neither mutational load nor CNV load, as a single component, was significantly associated with patient survival (Figures 1A and 1B). However, patients with low ITH had significantly better survival (Figure 1C), consistent with previous observations (Brown et al., 2014; Morris et al., 2016). Indeed, when patients were segregated by number of clones, distinct survival curves could be seen; patients with low ITH levels (2 clones) had the best survival rate, whereas those with high ITH levels (6 clones) had the worst survival rate (Figure 1D). When combining all three factors, we found that patients with a high ITH and a low mutational or CNV load had the worst survival rate (Figures 1E and 1F). These conclusions hold when controlling for potential confounding factors, including age, tumor stage, and tumor purity (STAR Methods). Finally, for each patient we computed the "cytolytic score (CYT)" (Rooney et al., 2015), which is associated with the degree of anticancer immunity based on the geometric mean expression of two key cytolytic effectors, Granzyme A and Perforin-1, which are upregulated upon CD8+ T cell activation and upon effective immunotherapy treatment. CYT scores were significantly higher in patients with low ITH compared with those with high ITH (Figure 1G; Wilcoxon rank-sum test, $p = 4.32 \times 10^{-6}$). Notably, the CYT scores were inversely correlated with the degree of number of clones throughout the TCGA cohort (Figure 1H; Spearman's rho = -0.27, $p = 4.3 \times 10^{-6}$). Together, our results clearly demonstrate that melanoma ITH plays a role in patient survival.

Establishing an *In Vivo* Mouse System to Uncouple TMB and ITH

Following these retrospective association results in human patients, we sought to establish an experimental *in vivo* mouse system that would enable us to uncouple TMB and ITH and study their influence on tumor immunogenicity in a causal, systematic manner. First, to assess the effect of increased mutational load and increased concomitant heterogeneity on anti-tumor immunity, we exposed the mouse melanoma B2905 cell line (Patel et al., 2017) to UVB irradiation (Figure 2A), a key carcinogenic source driving melanoma initiation (De Fabo et al., 2004). Because the literature regarding UVB research in melanoma varies considerably with respect to the amount of radiation exposure needed to induce melanoma genesis, we first titrated the amount of radiation needed for an optimal UVB response without compromising cell longevity. We found that a UVB dose of 600 J/m^2 was sufficient to induce p53 elevation (Budden et al., 2016) and cyclobutane pyrimidine dimer (CPD) formation (Chen et al., 2014) while maintaining the longevity of the murine melanoma cell lines B2905 and B16F10.9 (Figures S2A and S2B).

As expected, whole exome sequencing (WES) of these samples revealed that the TMB had increased by 2,734 exonic mutations (Table S1). The number of C > T transversions, a hallmark of melanoma, had also risen (Table S2) (Viros et al., 2014; Figure S2C), as had the UVB-grounded signature 7 (Alexandrov et al., 2013; Figure S2D). In parallel with the increase in TMB upon UVB irradiation, we also detected an increase in ITH from the distribution of the variant allele frequency (VAF; the frequency of a mutation within the population plotted against the probability density function), which was skewed toward a more subclonal phenotype (VAF < 0.25) (Williams et al., 2016) and exhibited a relatively small fraction of clonal single-nucleotide variants (SNVs): 0.063 compared with 0.079 in the parental cell line (Table S1; Figure 2B).

UVB-irradiated B2905 cells grew at a slower rate *in vitro* compared with non-irradiated B2905 cells (Figure S2E), the
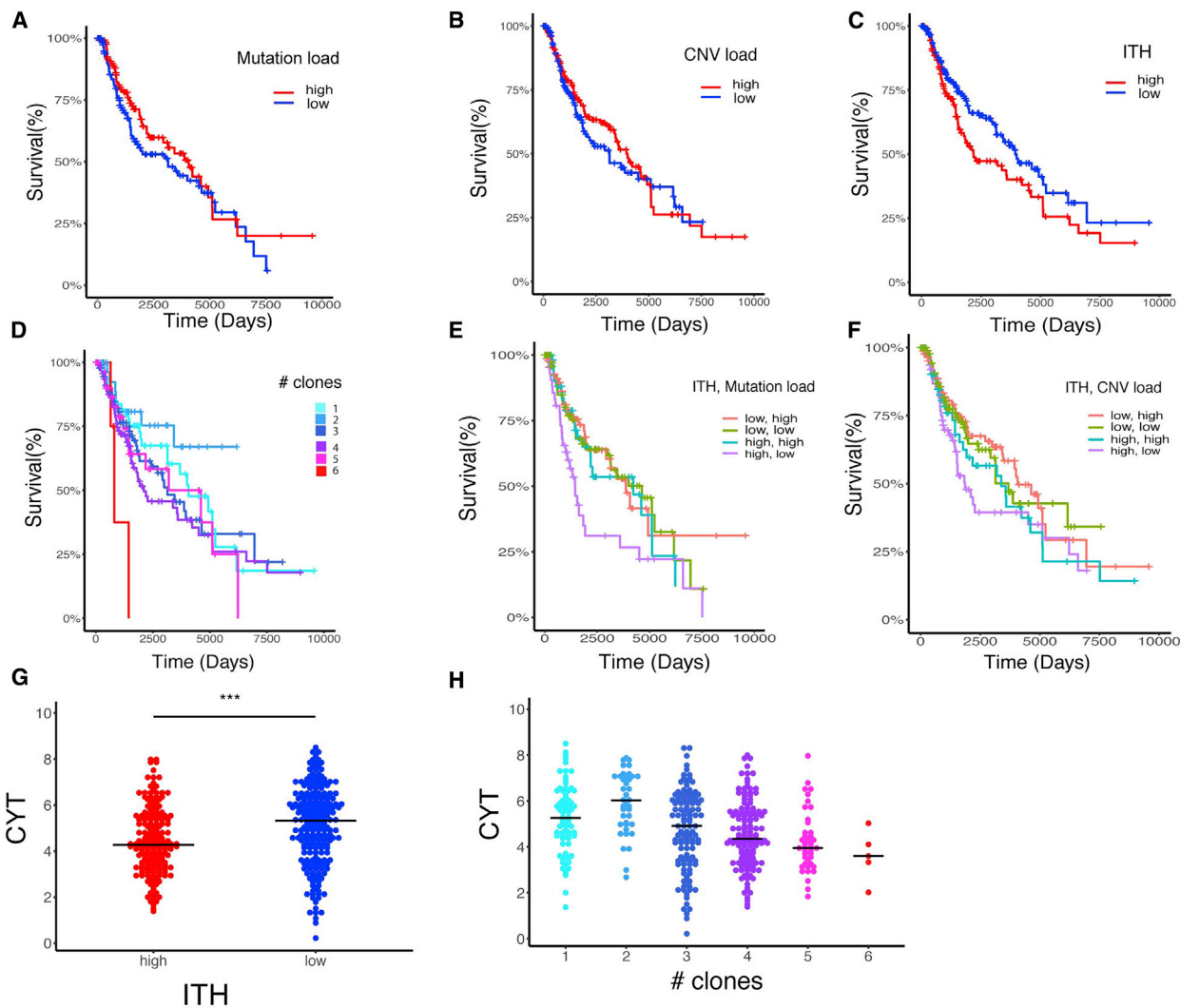
Figure 1. Analysis of the Association between ITH, Mutational Load, and Patient Survival across TCGA Skin Cutaneous Melanoma Samples

(A) Kaplan-Meier survival curves (time is measured in days on the x axis) of patients with high versus low mutational load. Log rank statistics: 1.96, p = 0.16.

(B) Kaplan-Meier survival curves of patients with high versus low CNV load. Log rank statistics: 0.31, p = 0.577.

(C) Kaplan-Meier survival curves of patient with high versus low ITH. Log rank statistics: 3.97, p = 0.046.

(D) Kaplan-Meier survival curves for patients segregated by their number of clones.

(E) Kaplan-Meier survival curves of patients segregated based on the combination of mutational load and ITH. Log rank statistics: 9.2, p = 0.0267.

(F) Kaplan-Meier survival curves of patients segregated based on the combination of CNV load and ITH. Log rank statistics: 4.57, p = 0.206.

(G) CYT score (in log scale) of patients with high versus low ITH. ***p < 0.001, Wilcoxon's test.

(H) CYT score (in log scale) of patients segregated by their number of clones. Spearman's rho: −0.27, p < 0.001.

For further information regarding the analyses, please refer to STAR Methods and Figure S1.

irradiated cell line gave rise to tumors with an increased growth rate when transplanted into immunocompetent syngeneic mice (Figures 2C and 2D). This effect was not cell line specific because irradiated B16F10.9 cells showed the same pattern of reduced growth *in vitro* (Figure S2F) and increased tumorigenicity *in vivo* (Figures S2G and S2H).

We then assessed whether tumors derived from these two lines, parental B2905 and UVB-irradiated B2905, had a differential response to PD-1 blockade. We found that the response of mice with the UVB-irradiated cell line to anti-PD-1 treatment was considerably milder than the response of those with parental

B2905 cells (Figure S2I). Given that the UVB signature cannot predict checkpoint blockade response in melanoma patients (Miao et al., 2018b) and that excessive TMB did not reduce tumor growth, we hypothesized that differences in heterogeneity may play a role in mediating tumor growth *in vivo*.

Lower Tumor Heterogeneity Leads to Decreased Tumor Growth

To discriminate between the functional effects of ITH and TMB, we assessed the cell growth and immunogenicity of melanoma cells with low ITH but distinct TMB levels. This involved
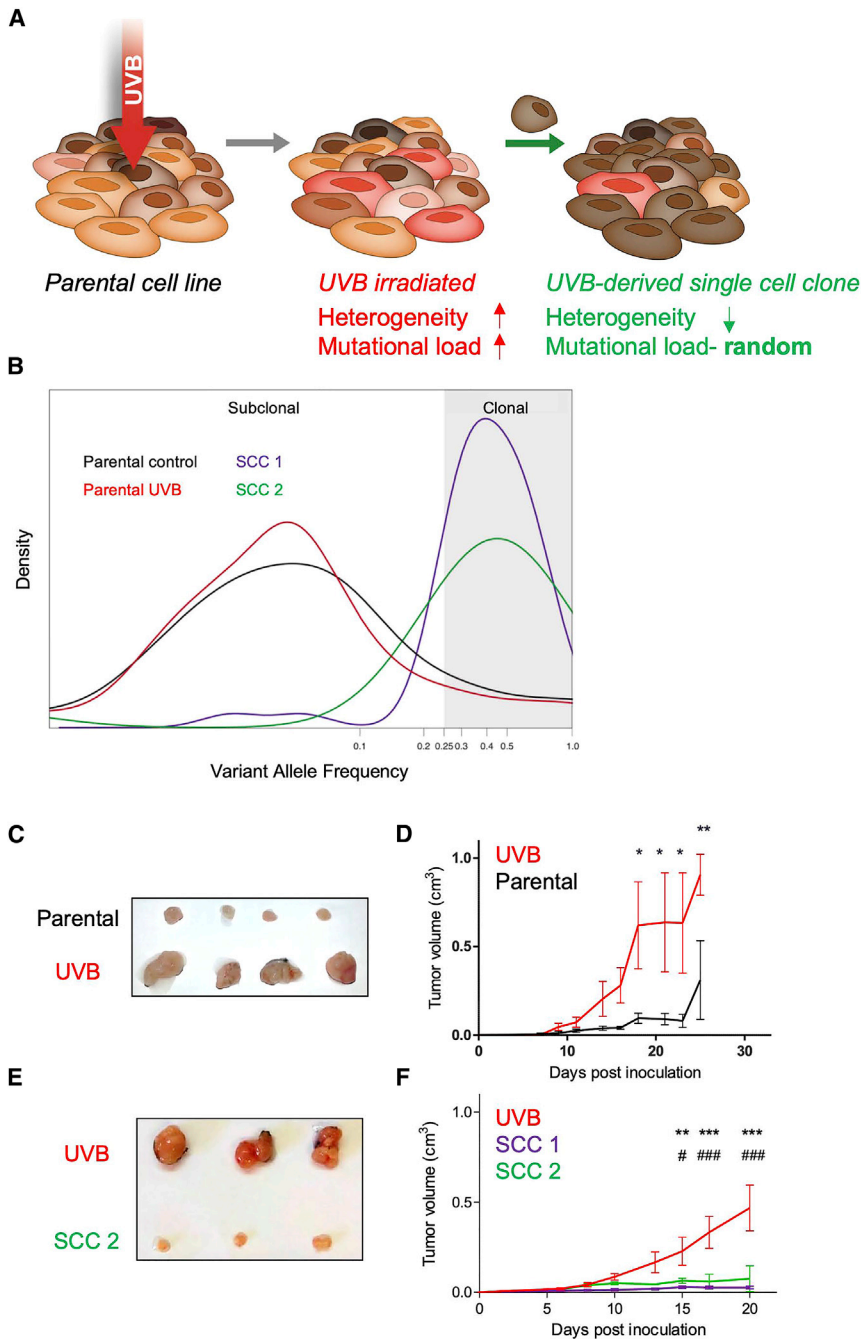
Figure 2. Differential Heterogeneity Induces Differential Tumor Growth *In Vivo*

(A) Scheme of experimental design for generating UVB-irradiated cells and generating SCCs derived from UVB-irradiated cells. Cell lines are irradiated by UVB at dosage of 600 J/m^2; from these irradiated cells, SCCs are generated.

(B) Distribution of variant allele frequencies (VAFs) of parental B2905 cells (black), UVB-irradiated B2905 cells (red), SCC 1 (purple), and SCC 2 (green) in log2 space. VAF > 0.25 (log2 = −2) is considered clonal.

(C) Tumors excised from mice inoculated with either parental or UVB-irradiated cell lines on day 15 after inoculation.

(D) *In vivo* tumor growth in mice inoculated with parental B2905 cells (black) and UVB-irradiated cells (red). n = 3–4; data are representative of three independent experiments. Data are mean ± SEM. *p < 0.05, ***p < 0.001, two-way ANOVA followed by Bonferroni's post hoc test.

(E) Tumors excised from UVB-irradiated B2905 cells versus SCC 2, day 19.

(F) *In vivo* growth of tumors in mice inoculated with UVB (red) or SCC 1 (purple) and SCC 2 (green). n = 4–5; data are representative of two independent experiments. Data are mean ± SEM. **p < 0.01***p < 0.001, two-way ANOVA followed by Bonferroni's post hoc test. * refers to UVB and SSC 1 comparisons; # refers to UVB and SSC 2 comparisons. See also Figure S2, Table S1, and Table S2.

ranging from 3,600 to 16,977 somatic mutations (Table S1). Unlike the UVB-irradiated parental cells, the two SCCs grew at a dramatically reduced rate *in vivo* and did not show an aggressive phenotype (Figures 2E and 2F; Figure S2K), suggesting that low ITH levels are associated with reduced aggressiveness.

To further explore these findings, we generated and inoculated 20 additional UVB-exposed B2905 SCCs into immunocompetent wild-type (WT) mice. We found that, despite the fact that all SCCs grew *in vitro* (Figure S3A), none exhibited the aggressive phenotype of their original line, giving rise to small tumors that were spontaneously rejected within 2–3 weeks (Figure 3A; Figure S3B). These results further support an association between low ITH levels and reduced aggressiveness. The mutational load, clonal SNV fraction, and C > T fraction of all assessed SCCs are presented in Figure S3C and Table S1.

A possible explanation for the aggressive tumor growth of UVB-irradiated B2905 cells *in vivo* is the emergence of an escaper SCC within the highly heterogeneous cell population that drives the growth of the overall tumor (McGranahan and Swanton, 2017). If this is the case, then the clonal composition of the tumor should evolve over time and become more
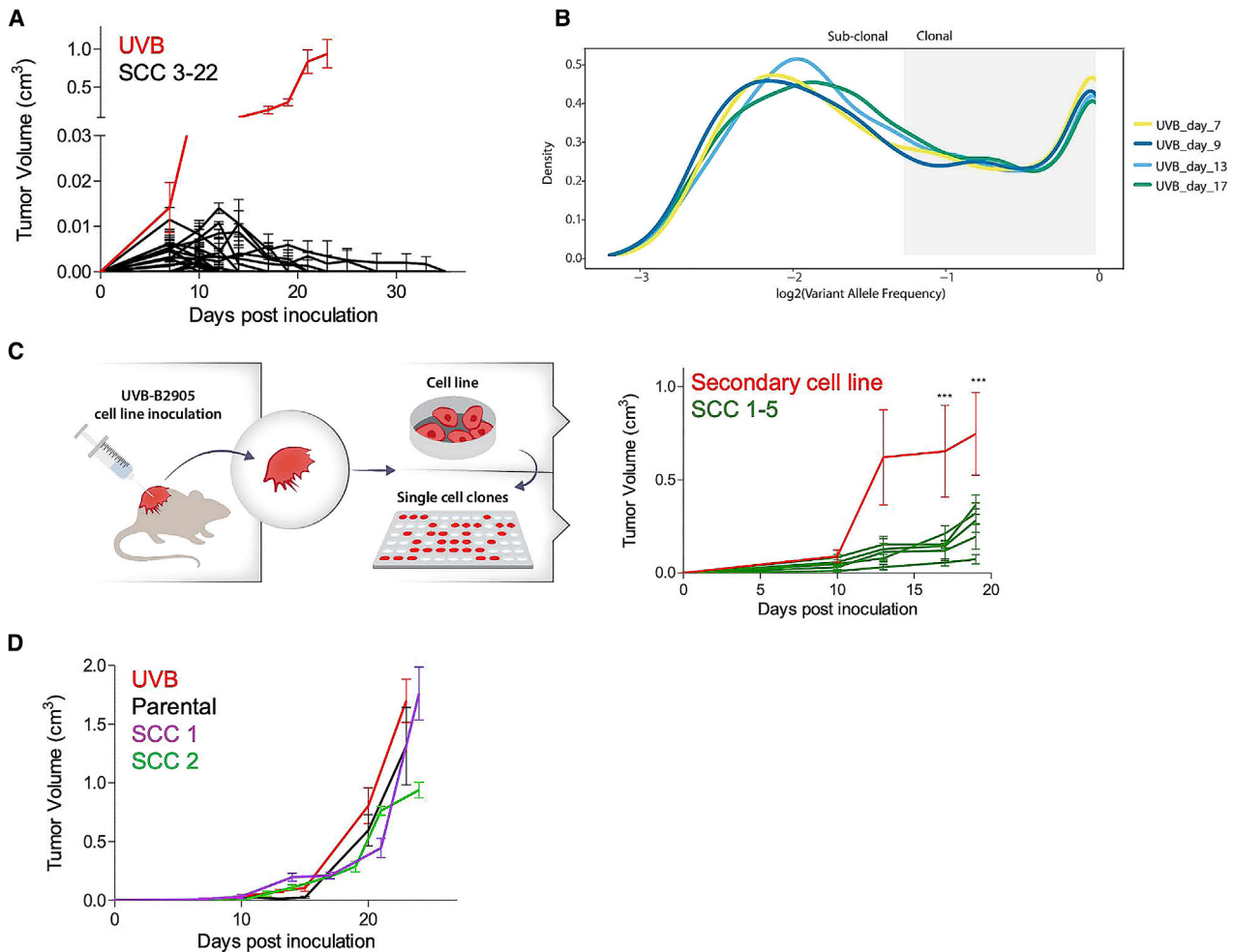
generating single-cell clones (SCCs) from UVB-irradiated B2905 cells (Figure 2A). We first generated and exome-sequenced two such B2905 clones, designated SCC1 and SCC2. Both clones harbored signature 7 mutations (Figure S2J), associated with UVB exposure and a much narrower clonal VAF distribution (SCC1 fraction of clonal SNVs = 0.846, SCC2 fraction of clonal SNVs = 0.887), testifying to significantly lower ITH levels than the origin cell line (Figure 2B). Importantly, the single-cell cloning procedure is stochastic, meaning that heterogeneity is dramatically reduced but the mutational load of the various SCCs varies,

Figure 3. Decreased Heterogeneity Correlates with Increased Anti-tumor Immune Response

(A) *In vivo* tumor growth in mice inoculated with the UVB-irradiated B2905 cell line (red, n = 5) or with 20 different SCCs derived from this line (SCC 3–22, black, n = 3). Data are representative of at least two independent experiments. Data are mean ± SEM.

(B) *In vivo* evolution experiment. Shown is a VAF plot for the UVB-irradiated B2905 line, generated from WES data of tumor samples taken on days 7, 9, 13, and 17 after inoculation. Data are representative of two biological repeats.

(C) Left: scheme of secondary cell line generation and its derivative SCCs. Right: *in vivo* tumor growth in mice inoculated with a secondary cell line derived from a UVB-irradiated B2905 inoculated tumor (red, n = 5) or with 5 different SCCs derived from this line (green, n = 5). Data are mean ± SEM. ***p < 0.001 in all SCC versus secondary cell line comparisons.
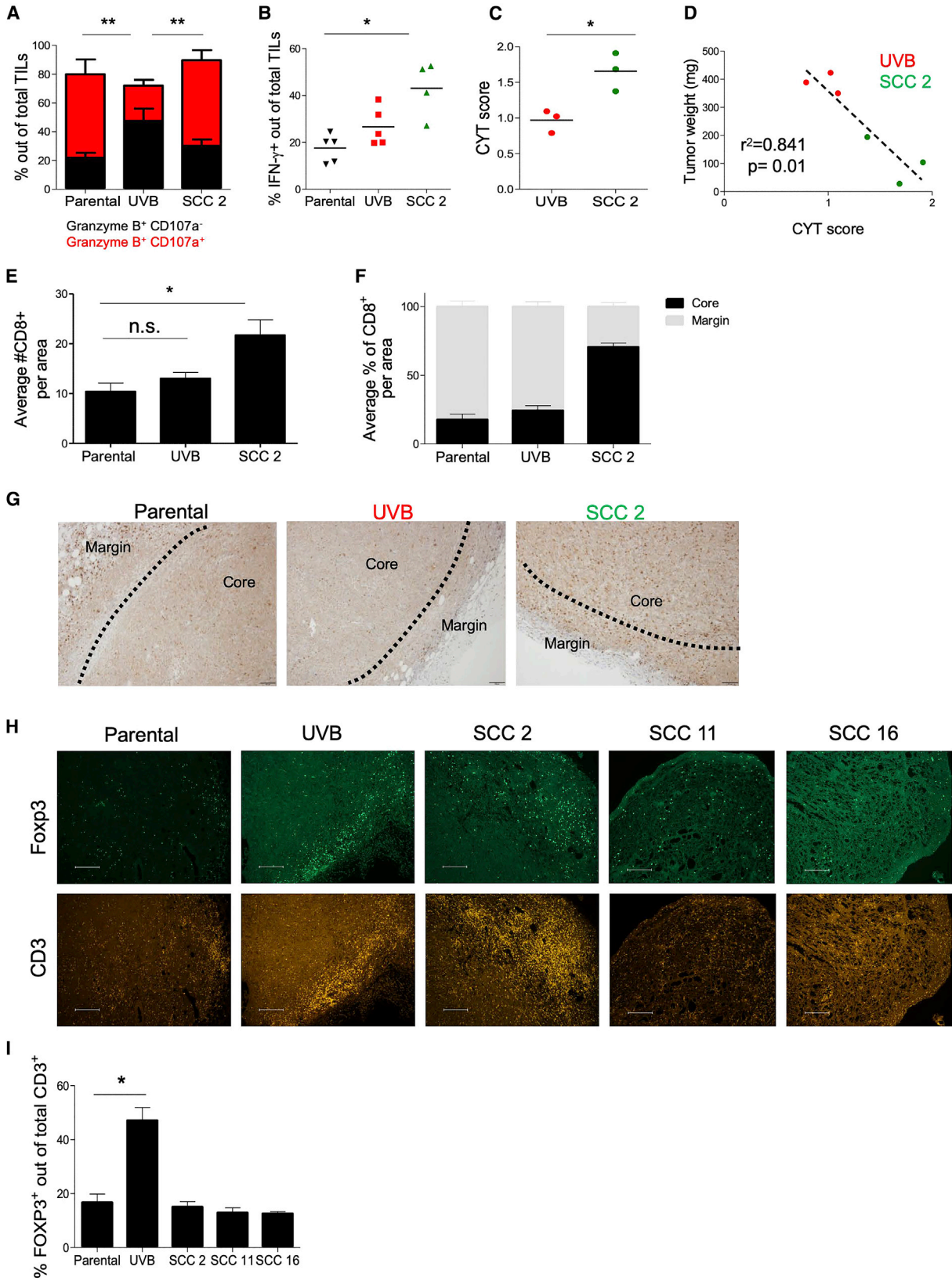
(D) *In vivo* tumor growth in NSG immunocompromised mice inoculated with the UVB-irradiated B2905 cell line (red, n = 3) or with SCCs derived from this line (SCC 1, purple, n = 4; SCC 2, green, n = 3) or with parental B2905 cells (black, n = 3). Data are mean ± SEM.

See also Figures S3 and S4.

homogeneous, and, thus, SCCs derived from the tumor should not be differentially immune rejected. This was assessed by monitoring the genetic composition of the UVB-irradiated tumors using WES of tumor samples taken at different time points after cell line inoculation. However, the clonal structure and heterogeneity remained stable even 17 days after inoculation, confirming that ITH levels did not change over time (Figure 3B). To further assess whether the aggressive tumor growth is sustained when inoculated as homogeneous individual SCCs, we generated ten SCCs from two secondary cell lines derived from two distinct UVB-irradiated tumors. As seen in Figure 3C and Figure S4A, eight of the ten SCCs grew less aggressively than their

respective parental cells, and none exceeded the aggressiveness of their respective parental cell line. Together, these data, showing that the vast majority of homogeneous SCCs are not aggressive and that the UVB-derived tumor remains genetically heterogeneous over time *in vivo*, suggest that the aggressiveness of the UVB-irradiated cell line cannot be solely explained by resistant subclones that outgrow the heterogeneous UVB-irradiated line.

To rule out that the differential growth phenotype between the UVB-irradiated line and the SCCs derived from it was due to the incidental occurrence of some specific UVB-induced mutations in this specific UVB-irradiated cell line,

we established two additional independent sets of UVB-irradiated B2905 lines (Figures S4B and S4C) and derived SCCs from them. As in the previous experiment, most of the SCCs (18 of 20) were rejected (Figures S4D and S4F). Importantly, all the generated SCCs grew well *in vitro*, similar to their cell of origin, UVB-irradiated B2905 cells (Figures S4E and S4G). These results recapitulate our findings with the previous UVB-irradiated cell line.

To identify the mechanisms underlying the *in vivo* growth differences between UVB-irradiated tumors with variable ITH levels, we focused on the first B2905 UVB-irradiated cell line. This cell line showed the most pronounced C > T alterations, the highest aggressiveness in comparison with the parental line, and a robust differential growth phenotype of all 22 non-aggressive SCCs derived from it. This forms the best setup for studying the effects of tumor heterogeneity on tumor growth in the clearest manner, with as few confounding factors as possible.

Reduced Growth of Low-Heterogeneity Tumors Is Due to Immune Rejection

The differences seen in tumor size between the parental cells, UVB-irradiated cells, and UVB-irradiated SCCs may result from different intrinsic growth rates *in vivo* or from an immune-dependent anti-tumor response. To investigate the latter, we tested the *in vivo* growth of parental and UVB-irradiated B2905 cells in immunocompromised non-obese diabetic.Cg-Prkdc^{scid}Il2rgt$^{m1Wjl/SzJ}$(NSG) mice. These mice are severely immunocompromised because they lack T, B, and natural killer (NK) cells and have impaired myeloid cells. In contrast to the differential growth in WT mice, there was no difference in growth rate between the three cell types in NSG mice (Figure 3D). This demonstrates that, indeed, the differences in growth of these cell lines are due to immune involvement. We further assessed the growth and immunogenicity of the tumors in a less immunocompromised context by inoculating the UVB-irradiated cell line and the two SCCs derived from it into CD80/86$^{-/-}$ double knockout mice that have intact T cells but are devoid of appropriate T cell stimulation (Bar-On et al., 2011) and are resistant to T cell-mediated autoimmunity (Wolf et al., 2018). Both clones exhibited considerably more aggressive growth in CD80/86$^{-/-}$ double knockout mice compared with

WT mice, testifying that they are indeed tumorigenic specifically in the absence of a T cell response (Figure S4H).

Decreased Heterogeneity Leads to Elevated T Cell Reactivity and Tumor Infiltration *In Vivo*

We next evaluated whether the growth rates of the tumors harboring different degrees of heterogeneity are mirrored by the degree of T cell reactivity *in vivo*. This was assessed by extracting total T cell receptor β^+ (TCRβ^+) TILs (tumor-infiltrating lymphocytes) from non-irradiated parental B2905 tumors, UVB-irradiated B2905-derived tumors, and B2905 SCC 2-derived tumors. To assess T cell reactivity, we measured the fraction of TILs positive for the cytotoxic mediator Granzyme B coupled with expression of CD107a, a degranulation marker (Alter et al., 2004; Rollman et al., 2007). Although total Granzyme B$^+$ fractions were similar in TILs derived from all tumors, the Granzyme B$^+$ CD107a$^+$ fraction of TILs was significantly reduced in UVB-irradiated B2905-derived tumors, whereas it remained similar in both the parental and the SCC 2-derived tumors (Figure 4A; Figure S5A). In addition, SCC 2-resident TILs contained a much higher interferon-γ^+ fraction (Figure 4B; Figure S5B), indicating stronger TIL activation and cytotoxicity. To substantiate these results, we sorted CD8$^+$ TILs from UVB-derived and SCC 2-derived tumors 16 days after inoculation, performed RNA sequencing (RNA-seq), and analyzed the TILs for their CYT score. CD8$^+$ TILs isolated from SCC 2-derived tumors had a higher CYT score, recapitulating the high CYT scores of the low-ITH TCGA melanoma patients (Figures 1G and 1H). Furthermore, this score significantly correlated with tumor weight (Figures 4C and 4D). Thus, the SCC 2-derived tumors, which had low ITH and were ultimately rejected *in vivo*, were more immunogenic than their parental heterogeneous UVB-irradiated, aggressive B2905-derived tumors, which had high ITH.

In addition to the immune composition of the tumor microenvironment, the spatial distribution of TILs within the malignant mass, in particularly immune infiltration into the tumor core, correlates with better survival and treatment success (Kather et al., 2018; König et al., 2019). Immunohistochemistry (IHC) and immunofluorescence analyses of tumor sections revealed that, although tumors derived from all three cell lines accumulated CD8$^+$ TILs in the tumor margin, those derived from SCC 2 featured both higher penetration of CD8$^+$ cells (Figure 4E) and

---

Figure 4. Homogeneous SCCs Elicit a Strong Immune Response

(A) Flow cytometry analysis of the Granzyme B and CD107a population in total TCRβ^+ TILs on day 19. n = 4–5; data are mean ± SEM. **p < 0.01 for Granzyme B$^+$ CD107a$^+$ TILs, two-way ANOVA followed by Bonferroni's post hoc test.

(B) Flow cytometry analysis of interferon-γ (IFN-γ) in total TILs on day 19. n = 4–5, *p < 0.05, Kruskal-Wallis test followed by Dunn's multiple comparisons test.

(C) CYT score derived from RNA-seq data of sorted CD8$^+$ TILs from UVB-irradiated B2905 and SCC 2 tumors on day 15. *p < 0.05, Mann-Whitney *U* test.

(D) Pearson correlation between CYT score and weights of tumors in Figure 3C.

(E) Quantitation of total CD8$^+$ TILs in the indicated tumors. Four sections from each tumor and three tumors derived from each cell line were examined. A significant difference was observed between parental cells and SSC 2 but not between parental cells and UVB. Data are mean ± SEM. *p < 0.05, one-way ANOVA followed by Tukey's post hoc test.

(F) Relative quantitation of the average percentage of CD8$^+$ TILs in the tumor core versus the margin of the tumors described in (E). Data are mean ± SD.

(G) Representative immunohistochemical stain for CD8 in slides taken from tumors derived by parental, UVB and SCC 2 on day 10 after cell inoculation. The scale bars represent 100 μM.

(H) Immunofluorescence stains of CD3 and Foxp3 in tumors derived from B2905 parental, UVB, and SCC 2, 16, and 11 on days 10−11 after cell inoculation. 3–4 sections from each tumor and two tumors derived from each cell line were examined. The scale bars represent 200 μM.

(I) Relative quantitation of the percentage of Foxp3$^+$ of CD3$^+$ TILs described in (H). Data are mean ± SEM. *p < 0.05, one-way ANOVA followed by Tukey's post hoc test. See also Figure S5.

massive infiltration of TILs into the tumor core (Figures 4F and 4G; Figures S5C and S5D). We recapitulated these data in three additional SCCs that also formed tumors large enough for IHC analysis (Figures S5E–S5G). We next quantified the levels of regulatory T cells (Tregs), which are known to suppress anti-tumor immunity and promote tumor growth (Arce Vargas et al., 2017; Tanaka and Sakaguchi, 2017) by CD3$^+$ Foxp3$^+$ immunofluorescence (IF) staining of these tumors and found a direct correlation between ITH and Treg levels (Figures 4H and 4I). In conclusion, low-ITH tumors show enhanced CD8$^+$ T cell infiltration to the tumor core, a lower presence of immunosuppressive Tregs, and higher degranulation and cytotoxicity compared with high-ITH tumors. This indicates that, indeed, low-ITH tumors elicit a strong anti-tumor response, whereas high ITH tumors are relatively non-immunogenic.

Detection of Reactive Neoantigens in Single-Cell-Derived Clones Using Immuno-peptidomics

To evaluate whether the high immunogenicity and T cell infiltration observed in tumors derived from SCCs is at least in part due to the presentation of immunogenic neoantigens, we employed immuno-peptidomics (Kalaora et al., 2016, 2018) to identify tumor-specific neoantigens in the various UVB-irradiated B2905-established SCC lines. This entailed purifying major histocompatibility complex (MHC) molecules by immunoaffinity and then analyzing the MHC-eluted peptides by capillary chromatography and tandem mass spectrometry (MS). Using this approach (STAR Methods), we identified a total of 18 neoantigens (Table S3) on 15 SCCs (synthetic peptides had a similar mass spectrum, indicating appropriate identification) (Figure S6A; STAR Methods). Thus, single-clone-specific neoantigens can be detected and might facilitate the anti-tumor immune response.

To further characterize the 18 identified neoantigens, we experimentally evaluated their binding to the two murine MHC class I alleles present on the C57/B6 background, H2-Db and H2-Kb, by incubating 11 predicted binders with the TAP-2-deficient lymphoma cell line RMA-S, which can express stable MHC class I only upon peptide binding (Lladser et al., 2010). Using this approach, we identified seven neoantigens that bound H2-Db and two that bound H2-Kb (Figure 5A; Figure S6B).

To test the *in vivo* reactivity of the three strong MHC class I binding neoantigens, we performed dendritic cell (DC)-mediated immunization against these three mutant peptides followed by an *in vivo* killing assay (Barber et al., 2003). For this, we used peptide-loaded, syngeneic bone marrow-derived DCs, validated as CD11c$^+$CD80$^+$CD86$^+$MHCII$^+$CCR7$^+$ (Figure S6C). We then used CD45.1$^+$ splenocytes loaded with either the mutant peptide (labeled with a high concentration of CFSE), WT peptide (labeled with a low concentration of CFSE) or unloaded splenocytes (labeled with a medium concentration of CFSE) and injected them at a 1:1:1 ratio (Figure S6D) into immunized mice. Twenty-four hours after splenocyte injection, specific killing was measured. As seen in Figure 5, the three neoantigen peptides induced between 17%–67% specific killing *in vivo*. This suggests that these neoantigens can indeed induce anti-tumor cytotoxicity *in vivo*, albeit at different levels of efficiency.

In conclusion, we identified 18 neoantigen peptides presented on MHC class I derived from 15 different clones and validated the *in vivo* reactivity of three of them. Our findings suggest that UVB-irradiated tumors do present neoantigens that can potentially mediate tumor cell killing by cytotoxic cells. However, within the vast heterogeneity of the UVB-irradiated cell line, these reactive peptides may be unable to mediate tumor elimination. In contrast, the robust rejection of the single clone-derived tumors *in vivo*, which have low ITH, is at least in part due to an enhanced immune response, as illustrated by the elevated levels of cytotoxicity and effector cytokines, detection of neoantigens, and successful infiltration of immune cells into the tumor core.

Systematic Clone Mixture Experiments Show that Both the Number of Clones and Their Genetic Diversity Mediate Tumor Growth and Rejection

To study the role of ITH in tumor rejection, we systematically generated tumors with defined states of heterogeneity using different combinations (mixtures) of the above-described 20 SCCs that were derived from the original, highly heterogeneous UVB-irradiated cell line. The individual SCCs were mixed in a controlled manner to dissect the functional ramifications of the two fundamental components of tumor heterogeneity: (1) the number of clones comprising the tumor and (2) the genetic diversity between them.

To choose relevant clones for the mixing experiments, we performed a phylogenetic analysis of the heterogeneous UVB cell line (STAR Methods). This yielded a phylogenetic tree with six terminal branches (TBs), numbered TB-4 to TB-10 (Figure 6A). An almost identical clustering was obtained using an orthogonal analytical methodology (Figure S7). We then placed the 20 SCCs on the various terminal branches of the tree, based on their sequence similarity. To study the role of tumor diversity in determining tumor growth, we inoculated four different mixtures of 3 SCCs and monitored their growth, as shown in Figure 6B. To achieve genetically diverse mixes, each mix contained clones from 3 different TBs of the UVB-irradiated phylogenetic tree (denoted as across branches [3AB]) (Figures 6B and 6E). As seen in Figure 6B, although diverse, none of the 3 clone mixes formed a large tumor, even 35 days after the mixes were inoculated. However, increasing the number of branches included in the mix from 3 to 6 (one clone from each TB [6AB]; Figure 6E) results in significantly larger tumors (Figures 6B and 6C) (group factor p = 0.0238 when 6AB is compared with the 3AB mixes by two-way ANOVA versus group factor p = 0.1614 when the 3AB mixes are compared without 6AB). Doubling the number of clones included from each of the six TBs (two clones from each TB [12AB]) further increased the subclonal/clonal mutation ratio (Figure 6D) and produced even more aggressive tumors (Figure 6C).

We next evaluated the functional effects of the tumor's genetic diversity while controlling for the overall mutational load. To this end, we compared the growth of tumors generated from a mixture of clones originating from a single TB (6 SCCs within TB-4 [6WB]) with that of those generated from the 6AB mix described above (comprising clones from TB-4, TB-6, TB-7, TB-8, TB-9, and TB-10) (Figures 6C and 6E). These two mixes have the same number of clones (six) and approximately the
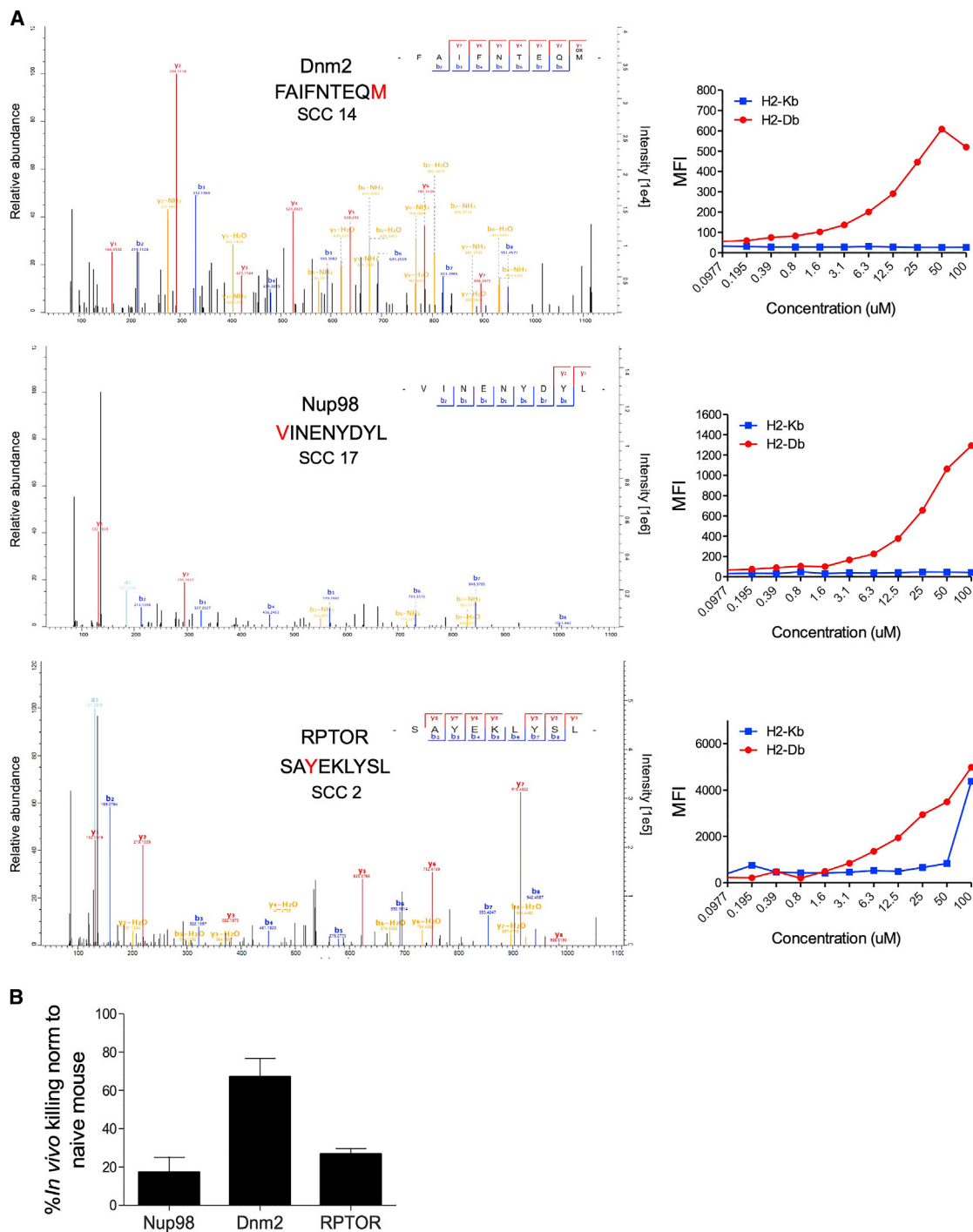
Figure 5. Detection and Characterization of HLA-Bound Neoantigens in SCCs

(A) Left: spectra of three representative neoantigens detected by targeted mass spectrometry. The SCCs in which these neoantigens were detected are indicated. Right: surface expression of H2-D_b and H2-K_b on RMA-S cells incubated with the peptides at 0.1–100 μM for 18 h and measured by flow cytometry analysis.

(B) *In vivo* killing assay in mice immunized with the three neoantigens described in (A) using DC vaccination. The killing percentage is calculated relative to the killing measured in naive, non-vaccinated mice.

n = 2–3. Data are mean ± SEM. See also Figure S6 and Tables S2 and S3.
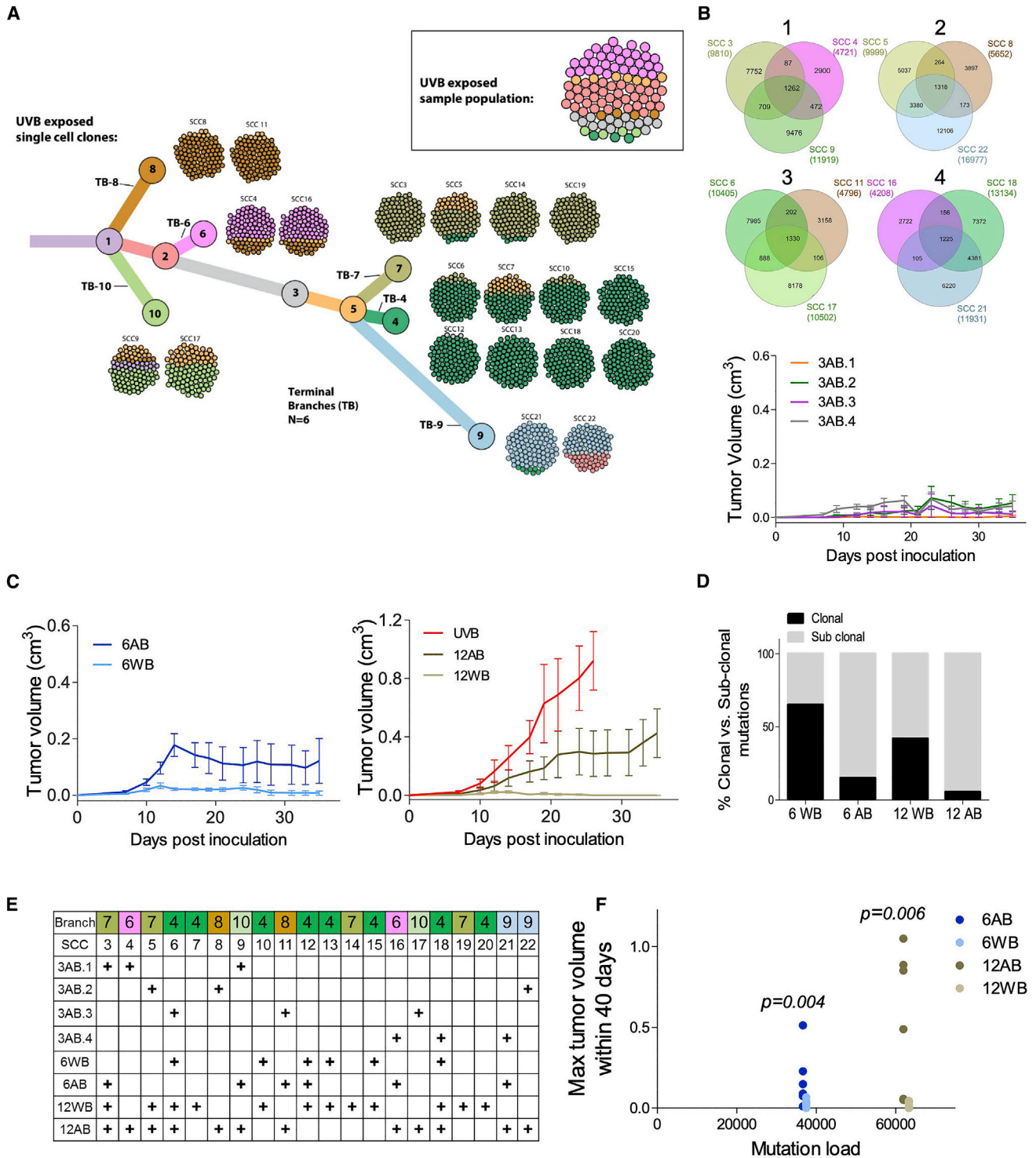
Figure 6. Tumors Derived from Mixtures of Clones Show Differential Growth *In Vivo*

(A) Phylogenetic tree representation of the UVB-irradiated B2905 cell line. The tree depicts the results from mutation clustering analysis, which was used to define the distinct subclones present within the UVB cell line. The phylogenetic relationship between subclones is shown, and then each of the 20 UVB derived SCCs is mapped onto the subclonal branch with the highest genetic similarity. Each of the 20 SCCs is depicted as a ball of 100 tumor cells, with the color coding reflecting the percentage frequency of each branch in each SCC sample. Shown in the top right box is a representation of the UVB parental sample, again shown as a ball of 100 tumor cells, color-coded to match the subclonal branches. See also Figure S7.

(legend continued on next page)

same mutational loads (Figure 6F) but vary in their genetic diversity, as assessed by their clonal versus subclonal mutation ratios (Figure 6D). Despite having similar mutational loads, we identified striking differences in growth between 6AB and 6WB (Figure 6C). Similarly, we next compared the tumor growth curves of a mixture of 12 SCCs derived from one branch (12WB, derived from branch 5, which contains TB-4 and TB-7) with the growth of the 12AB mix (two SCCs from TB-4, TB-6, TB-7, TB-8, TB-9, and TB-10) (Figures 6C and 6E). Again, there were clear differences in tumor growth between 12AB and 12WB. Moreover, even though 12AB had a higher mutational load than 6AB (Figure 6D), its growth surpassed that of 6AB. This indicates that an increased mutational load is not sufficient to drive tumor rejection. The 12AB tumors were still not as aggressive as the UVB irradiation-derived tumors (Figure 6C), emphasizing that the latter tumors harbor a higher degree of ITH. Taken together, these results testify that both the number of tumor subclones and their genetic diversity play important roles in mediating tumor growth and rejection.

Tumor Clonal Diversity Is Associated with Overall Survival in Checkpoint Inhibitor-Treated Melanoma Patients

To further evaluate the extent to which the number of clones and their genetic diversity affect the anti-tumor immune response in human data, we analyzed four previously published melanoma checkpoint inhibitor cohorts from Snyder et al. (2014), Riaz et al. (2017), Hugo et al. (2016), and Van Allen et al. (2015). Given the results of the mixing experiment that show that both the number of clones and their diversity are important determinants of tumor growth, we analyzed patient data using the Shannon diversity index (SDI), a formal diversity metric that quantitatively measures both the number of clones and the diversity of the mutations across clones in one index. As an example, a tumor with a low SDI would have nearly all of its mutations concentrated in just one clone (a large truncal neoantigen burden). In contrast, a high-SDI tumor would have a high number of clones with mutations spread evenly or diversely across each clone (a large branched neoantigen burden) (Figure 7A). The first cohort analyzed (Snyder et al., 2014) comprised data from 54 patients treated with anti-CTLA-4 therapy. We found its SDI index to significantly associate with overall survival (p = 0.0064, SDI tested as a continuous variable, z-test from the Cox proportional hazard model; Figures 7B and 7F). Patients with a higher diversity tumor (as measured by SDI) had poorer survival, with a hazard ratio (HR) of 8.8 (95% confidence interval, 1.8–41.6) per unit increase in SDI (Figure 7F). In the second cohort (Riaz et al., 2017), containing 57 patients treated with anti-PD1 therapy, we

observed a comparable but non-significant pattern (p = 0.079, HR = 2.2 [0.9–5.5] per unit increase in SDI (Figures 7C and 7F). In the third cohort (Hugo et al., 2016), composed of 21 patients treated with anti-PD1 therapy, again a comparable but non-significant pattern was noted (p = 0.096, HR = 4.2 [0.8–23.8] per unit increase in SDI; Figures 7D and 7E). In the final cohort, which had data available from 70 patients treated with anti-CTLA4 therapy, no significant association between SDI and overall survival was detected (Figures 7E and 7F); it should be noted, however, that this result is consistent with previous ITH analyses in this cohort (McGranahan et al., 2016) and may be explained by the high level of pre-treatment in this cohort, making biomarker analyses more challenging. Given that all four datasets are of fairly limited size, we performed a meta-analysis across all four studies, which yielded an overall significance value of P_{meta} = 0.0105, testifying that clone number and genetic diversity between clones are drivers of the immunotherapy response in human cohorts. Importantly, this result remained significant after adjusting for tumor purity in a multi-variable analysis for each cohort, with updated P_{meta} = 0.012 for the SDI variable (across all four studies), and P_{meta} = 0.15 for tumor purity, suggesting that the latter is not a confounding variable in our analysis (Table S4). Similarly, we corrected for TMB in the multi-variable analysis for each cohort, which yielded an updated P_{meta} = 0.039 for the SDI variable and P_{meta} = 0.33 for TMB (Table S5).

DISCUSSION

Here we have established an experimental system that enables one to tease apart and study the effect of TMB and ITH on tumor aggressiveness, evaluating their influence on anti-tumor immunity in a controlled manner. Our findings in mice suggest that, in melanoma, an essential genetic determinant of anti-tumor immune response is tumor heterogeneity. These results corroborate previous reports that clonal neoantigens are associated with a more robust tumor infiltrate and clinical outcome, with and without checkpoint inhibitor blockade (McGranahan et al., 2016). By systematically generating tumors composed of different SCC mixes in a designed, controlled manner, we further dissected the two major components of a tumor's ITH, finding that both the number of distinct clones composing the tumor and the degree of their genetic diversity influence tumor aggressiveness.

Our experimental mouse data are mirrored in TCGA melanoma patients, where the overall survival rate is significantly higher in tumors with a fewer number of clones, and the combination of number of clones and diversity (their SDI) is inversely

(B) Top: Venn diagrams for the four 3AB mixes inoculated, representing the number of protein-coding mutations and their intersections between the SCC in each mix. Bottom: in vivo tumor growth curves of the four different 3AB mixes. n = 5. Data are mean ± SEM.

(C) Left: in vivo tumor growth curves of the 6WB mix (within TB-4) and 6AB mix (one SCC from each TB). n = 4–5. Right: in vivo tumor growth curves of the 12WB mix (within TB-5) and 12AB mix (two SCC from each TB) and the UVB-irradiated B2905 cell line. n = 5–6. Data are mean ± SEM.

(D) Percent clonal versus sub-clonal mutations in the mixes described in (C).

(E) The SCC included in each mix described in (B) and (C).

(F) The association between the 6AB, 6AB, 12AB, and 12WB mix mutation number (unique) and the maximal tumor volume size (cubic centimeters) within 40 days. Each dot represents an individual mouse. The graph shows statistical significance between the 6 and 12 mixes but not between mutation number and tumor volume (Wilcoxon rank-sum test).
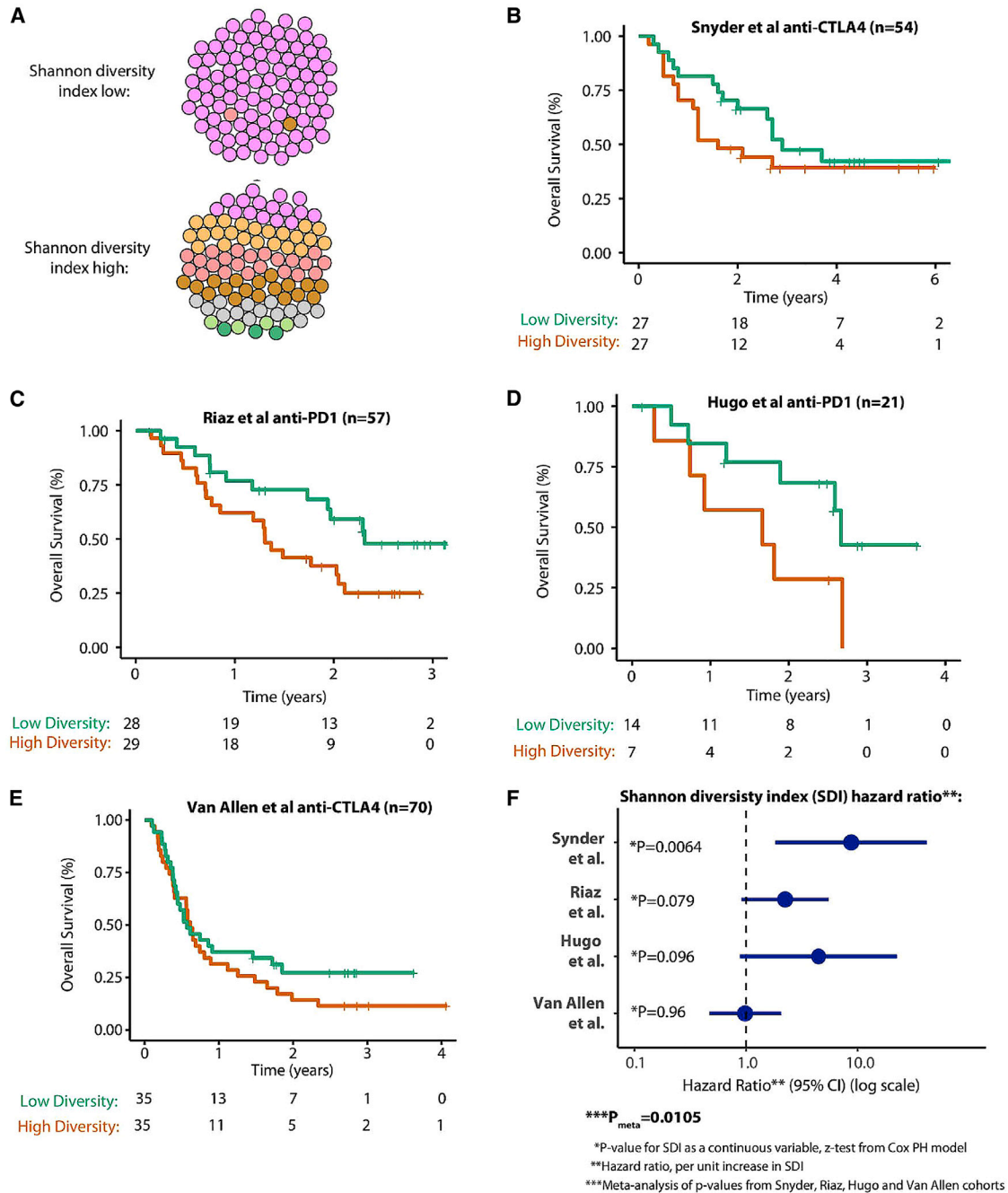
See also Table S7.

Figure 7. Shannon Diversity Index (SDI) Analysis in Immune Checkpoint Inhibitor Datasets

(A) The cartoon illustrates two examples of the SDI, top low SDI (the tumor is predominantly composed of one major clone) and bottom high SDI (the tumor is composed of multiple clones with higher evenness between clones). SDI is measured using individual tumor subclones (from Pyclone clustering) as types and the somatic mutations as entities so that a tumor with a low SDI would have nearly all mutations concentrated in just one clone, and, in contrast, a tumor with a high SDI would have a higher number of clones, with mutations spread evenly or diversely across each clone.

(B) The SDI analysis applied to the Snyder et al. (2014) anti-CTLA4 dataset. Overall survival Kaplan-Meier plots are shown for with patients with a high SDI in red (SDI above median value in cohort) and a low SDI in green. The number of patients at risk by time point is shown in the table below.

(C–E) The same data format as in (B) for the Riaz et al. (2017) anti-PD-1 dataset (C), Hugo et al. (2016) anti-PD-1 dataset (D), and Van Allen et al. (2015) anti-CTLA4 dataset (D), respectively.

(F) Forest plot showing the HR for the SDI in each dataset, with the HR value corresponding to the survival risk per unit increase (i.e., each +1 increment) in the SDI. For significance analysis, SDI is tested as a continuous variable (to show a continuous association across the full range of data) using a Cox proportional hazard model (other clinical predictors, e.g., stage, are not included).

See also Tables S4 and S5.

associated with overall survival in immune checkpoint inhibitor-treated cohorts. These findings, which tightly match our experimental findings in mice, further support the detrimental influence of tumor heterogeneity on the anti-tumor immune response in humans, in keeping with previous studies (McGranahan et al., 2016).

Alongside the effects on tumor growth and responsiveness, the complex mechanisms behind the modulation of anti-tumor immunity by tumor heterogeneity need to be further addressed in future studies. We suggest that diminishing tumor heterogeneity exposes tumor cells by reducing their neoantigen landscape, bringing reactive neoantigens to the "frontline," thus better exposing them to immune detection. This, in turn, leads to enhanced infiltration into the tumor core, elevated effector cytokines, and heightened degranulation. When neoantigen-specific CD8^{+} T cells are able to infiltrate and kill tumor cells, more tumor antigens are exposed to the tumor microenvironment, further promoting neoantigen uptake and presentation by tumor-associated DCs, enhancing the ability of the immune system to reject the tumor. In contrast, in more heterogeneous tumor cell populations, tumor cells could have a better chance of escaping immune surveillance because the reactive neoantigens undergo "dilution" within the tumor relative to other neoantigens. The total outcome is weaker anti-tumor immunity, manifested by reduced immune infiltration into the tumor core and dampening of TIL degranulation, cytotoxicity, effector cytokine secretion, and proliferation. In addition to CD8^{+} T cells, we found lower numbers of Tregs in tumors derived from SCCs (low ITH) than in UVB-derived, more heterogeneous tumors, indicating a strong immunosuppressive tumor microenvironment in high-ITH tumors that is resolved in single-cell-derived tumors. Overall, our results are consistent with the recent hypothesis by Gejman et al. (2018) that, because of increased antigenic variability, the relative expression of each neoantigen is lowered in tumors with increased ITH, diminishing the TILs' ability to home to their target cells and mount a sufficient cytotoxic response.

In addition to the differential infiltration of CD8^{+} T cells and differential Treg accumulation observed in the tumors, other immune mechanisms also likely play a part in the reduced response to heterogeneous versus homogeneous tumors. These may involve non-Treg CD4^{+} cells, which are important for priming of CD8^{+} T cells (Borst et al., 2018) and recognition of MHC class II-borne tumor antigens (Zanetti, 2015). Different CD4^{+} T cells effector subsets can have direct or indirect anti-tumor immunity. These subsets include CD4^{+} cytotoxic T cells that can directly eliminate MHC class II^{+} tumors (Haabeth et al., 2014) and CD4^{+} Th1 and Th17 cells that can mediate elimination of tumor cells in an antigen-specific manner (Muranski et al., 2008; Quezada et al., 2010). Indeed, strong anti-tumor responses of CD4^{+} cells against tumor MHC class II neoantigens in cancer patients have been reported (Linnemann et al., 2015; Tran et al., 2014; Veatch et al., 2018). This suggests an additional level of complexity within the tumor-immune interface and a significant clinical potential for future therapies.

Additional immune subsets other than T cells that may play a role in this setting encompass M1 and M2 macrophage polariza-

tion (Brown et al., 2017), NK cells (Guillerey et al., 2016) DCs (de Mingo Pulido et al., 2018), or neutrophils (Coffelt et al., 2015). To fully elucidate the immune profiles of ITH-high versus -low tumors, cutting-edge, high-dimensional techniques such as single-cell RNA-seq (Li et al., 2019; Sade-Feldman et al., 2018) and CyTOF (Gubin et al., 2018) and state-of-the-art analysis algorithms such as CIBERSORT (Newman et al., 2015) could be utilized in follow-up studies.

Although we show that high ITH impairs the immune system response, tumors with impaired immune responses can likely still acquire high levels of ITH. Thus, impaired immune response and ITH levels are tightly associated. However, whether ITH is a cause or a consequence of tumor progression or both is not fully elucidated. Interestingly, previous studies have shown that functional cooperation between genetically distinct subclones can be essential for overcoming environmental constraints and, thus, affect tumor maintenance and growth (Cleary et al., 2014; Marusyk et al., 2014) and metastatic behavior (Janiszewska et al., 2019). Of note, it has been shown recently that the immune system as well as checkpoint immunotherapy can select for low-ITH tumors (Milo et al., 2018). Understanding the complex interactions between tumor heterogeneity and the immune response and how they change during tumor evolution still remains a challenge.

Despite the strengths, there are several shortcomings of our study. Specifically, the single-cell cloning process inherently involves in vitro selection of clones. This may miss clones with a low survival capability in vitro, which does not necessarily reflect their functional importance in vivo. Likewise, we acknowledge the limitations of accurately assessing ITH from a single biopsy sample in the TCGA and immune checkpoint blockade (ICB) datasets because of the narrow sampling frame of taking just one sample from one spatial location. The sequencing depth, tumor purity, choice of processing pipeline, and nature of the single biopsy (primary versus metastatic) may also affect ITH assessment, making it challenging to derive a single prognostic measure of ITH. We believe that additional studies that quantify ITH in large-scale cohorts with multi-region biopsies are likely to shed further light on the prognostic role of tumor ITH, providing a higher-resolution view of the fundamental trends outlined in this study.

In summary, our findings show the value of evaluating ITH as an important determinant of melanoma patients' response to checkpoint therapy. They also support the notion that clonal neoantigens are more likely to lead to better cancer vaccines (McGranahan et al., 2016; Sahin and Türeci, 2018). On the flip side, our results cast doubt on the notion that excessive mutagenesis, directed to enhance TMB, can enhance the efficacy of immunotherapy. Indeed, it is conceivable that excessive neoantigen heterogeneity may actively impair a productive anti-tumor immune response. In conclusion, our functional data support recent findings that the clonality of a tumor can be used as a biomarker for predicting better outcomes in melanoma and may improve patient matching to current immunotherapy in a manner complementary to mutational load. We suggest that ITH is a strong determinant of immune response and immunotherapy success in melanoma, highlighting the potential importance of assessing it in the clinic.

STAR★METHODS

Detailed methods are provided in the online version of this paper and include the following:

- KEY RESOURCES TABLE
- LEAD CONTACT AND MATERIALS AVAILABILITY
- EXPERIMENTAL MODEL AND SUBJECT DETAILS
  - Mice
  - Cell lines
- METHOD DETAILS
  - UVB exposure
  - *In vitro* proliferation
  - Generation of single-cell clones
  - Western blotting
  - *In vivo* mouse experiments
  - Flow cytometry of TILs
  - RNA-sequencing
  - Secondary cell line generation, derived from UVB-B2905 solid tumors
  - Histology
  - CPD detection
  - DNA-Sequencing and analysis
  - Cancer Signature analysis
  - Genetic heterogeneity analysis of melanoma cell lines
  - Production and purification of membrane MHC molecules
  - Identification of the MHC peptides
  - Hydrophobicity calculation
  - RMA-S peptide binding assay
  - Inference of ITH, mutation and CNV load
  - TCGA Survival Analysis
  - Estimating cytolytic activity from RNA-seq data
  - Phylogenetic analysis of mouse UVB and SCCs
  - Shannon diversity index analysis
- QUANTIFICATION AND STATISTICAL ANALYSIS
- DATA AND CODE AVAILABILITY

SUPPLEMENTAL INFORMATION

Supplemental Information can be found online at https://doi.org/10.1016/j.cell.2019.08.032.

DECLARATION OF INTERESTS

C.S. declares the following receipt of grants/research support: Pfizer, AstraZeneca, BMS, Roche Ventana. Receipt of honoraria, consultancy, or SAB Member fees: Pfizer, Novartis, GlaxoSmithKline, MSD, BMS, Celgene, AstraZeneca, Illumina, Sarah Canon Research Institute, Genentech, Roche-Ventana, GRAIL, Medicxi Advisor for Dynamo Therapeutics. Stock shareholder: Apogen Biotechnologies, Epic Bioscience, GRAIL. Co-Founder & stock options: Achilles Therapeutics. K.L. reports speaker fees from Roche Tissue Diagnostics and patents pending on indel burden as a predictor of checkpoint inhibitor response and targeting of frameshift neoantigens for personalised immunotherapy.

REFERENCES

Alexandrov, L.B., Nik-Zainal, S., Wedge, D.C., Aparicio, S.A., Behjati, S., Biankin, A.V., Bignell, G.R., Bolli, N., Borg, A., Børresen-Dale, A.L., et al.; Australian Pancreatic Cancer Genome Initiative; ICGC Breast Cancer Consortium; ICGC MMML-Seq Consortium; ICGC PedBrain (2013). Signatures of mutational processes in human cancer. Nature *500*, 415–421.

Alter, G., Malenfant, J.M., and Altfeld, M. (2004). CD107a as a functional marker for the identification of natural killer cell activity. J. Immunol. Methods *294*, 15–22.

Andor, N., Graham, T.A., Jansen, M., Xia, L.C., Aktipis, C.A., Petritsch, C., Ji, H.P., and Maley, C.C. (2016). Pan-cancer analysis of the extent and consequences of intratumor heterogeneity. Nat. Med. *22*, 105–113.

Arce Vargas, F., Furness, A.J.S., Solomon, I., Joshi, K., Mekkaoui, L., Lesko, M.H., Miranda Rota, E., Dahan, R., Georgiou, A., Sledzinska, A., et al.; Melanoma TRACERx Consortium; Renal TRACERx Consortium; Lung TRACERx Consortium (2017). Fc-Optimized Anti-CD25 Depletes Tumor-Infiltrating Regulatory T Cells and Synergizes with PD-1 Blockade to Eradicate Established Tumors. Immunity *46*, 577–586.

Bar-On, L., Birnberg, T., Kim, K.W., and Jung, S. (2011). Dendritic cell-restricted CD80/86 deficiency results in peripheral regulatory T-cell reduction but is not associated with lymphocyte hyperactivation. Eur. J. Immunol. *41*, 291–298.

Barber, D.L., Wherry, E.J., and Ahmed, R. (2003). Cutting edge: rapid in vivo killing by memory CD8 T cells. J. Immunol. *171*, 27–31.

Bassani-Sternberg, M., Barnea, E., Beer, I., Avivi, I., Katz, T., and Admon, A. (2010). Soluble plasma HLA peptidome as a potential source for cancer biomarkers. Proc. Natl. Acad. Sci. USA *107*, 18769–18776.

Bolger, A.M., Lohse, M., and Usadel, B. (2014). Trimmomatic: a flexible trimmer for Illumina sequence data. Bioinformatics *30*, 2114–2120.

Borst, J., Ahrends, T., Bąbała, N., Melief, C.J.M., and Kastenmüller, W. (2018). CD4$^+$ T cell help in cancer immunology and immunotherapy. Nat. Rev. Immunol. *18*, 635–647.

Brown, S.D., Warren, R.L., Gibb, E.A., Martin, S.D., Spinelli, J.J., Nelson, B.H., and Holt, R.A. (2014). Neo-antigens predicted by tumor genome meta-analysis correlate with increased patient survival. Genome Res. *24*, 743–750.

Brown, J.M., Recht, L., and Strober, S. (2017). The Promise of Targeting Macrophages in Cancer Therapy. Clin. Cancer Res. *23*, 3241–3250.

Budden, T., Davey, R.J., Vilain, R.E., Ashton, K.A., Braye, S.G., Beveridge, N.J., and Bowden, N.A. (2016). Repair of UVB-induced DNA damage is reduced in melanoma due to low XPC and global genome repair. Oncotarget *7*, 60940–60953.

Cancer Genome Atlas Network (2015). Genomic Classification of Cutaneous Melanoma. Cell *161*, 1681–1696.

Chan, T.A., Yarchoan, M., Jaffee, E., Swanton, C., Quezada, S.A., Stenzinger, A., and Peters, S. (2019). Development of tumor mutation burden as an immunotherapy biomarker: utility for the oncology clinic. Ann. Oncol. *30*, 44–56.

Chen, H., Weng, Q.Y., and Fisher, D.E. (2014). UV signaling pathways within the skin. J. Invest. Dermatol. *134*, 2080–2085.

Chihara, N., Madi, A., Kondo, T., Zhang, H., Acharya, N., Singer, M., Nyman, J., Marjanovic, N.D., Kowalczyk, M.S., Wang, C., et al. (2018). Induction and transcriptional regulation of the co-inhibitory gene module in T cells. Nature *558*, 454–459.

Chowell, D., Krishna, S., Becker, P.D., Cocita, C., Shu, J., Tan, X., Greenberg, P.D., Klavinskis, L.S., Blattman, J.N., and Anderson, K.S. (2015). TCR contact residue hydrophobicity is a hallmark of immunogenic CD8+ T cell epitopes. Proc. Natl. Acad. Sci. USA *112*, E1754–E1762.

Cleary, A.S., Leonard, T.L., Gestl, S.A., and Gunther, E.J. (2014). Tumour cell heterogeneity maintained by cooperating subclones in Wnt-driven mammary cancers. Nature *508*, 113–117.

Coffelt, S.B., Kersten, K., Doornebal, C.W., Weiden, J., Vrijland, K., Hau, C.-S., Verstegen, N.J.M., Ciampricotti, M., Hawinkels, L.J.A.C., Jonkers, J., and de Visser, K.E. (2015). IL-17-producing γδ T cells and neutrophils conspire to promote breast cancer metastasis. Nature *522*, 345–348.

Cox, J., and Mann, M. (2008). MaxQuant enables high peptide identification rates, individualized p.p.b.-range mass accuracies and proteome-wide protein quantification. Nat. Biotechnol. *26*, 1367–1372.

Dang, H.X., White, B.S., Foltz, S.M., Miller, C.A., Luo, J., Fields, R.C., and Maher, C.A. (2017). ClonEvol: clonal ordering and visualization in cancer sequencing. Ann. Oncol. *28*, 3076–3082.

De Fabo, E.C., Noonan, F.P., Fears, T., and Merlino, G. (2004). Ultraviolet B but not ultraviolet A radiation initiates melanoma. Cancer Res. *64*, 6372–6376.

de Mingo Pulido, A., Gardner, A., Hiebler, S., Soliman, H., Rugo, H.S., Krummel, M.F., Coussens, L.M., and Ruffell, B. (2018). TIM-3 Regulates CD103(+) Dendritic Cell Function and Response to Chemotherapy in Breast Cancer. Cancer Cell *33*, 60–74.e6.

DePristo, M.A., Banks, E., Poplin, R., Garimella, K.V., Maguire, J.R., Hartl, C., Philippakis, A.A., del Angel, G., Rivas, M.A., Hanna, M., et al. (2011). A framework for variation discovery and genotyping using next-generation DNA sequencing data. Nat. Genet. *43*, 491–498.

Gejman, R.S., Chang, A.Y., Jones, H.F., DiKun, K., Hakimi, A.A., Schietinger, A., and Scheinberg, D.A. (2018). Rejection of immunogenic tumor clones is limited by clonal fraction. eLife *7*, e41090.

Germano, G., Lamba, S., Rospo, G., Barault, L., Magrì, A., Maione, F., Russo, M., Crisafulli, G., Bartolini, A., Lerda, G., et al. (2017). Inactivation of DNA repair triggers neoantigen generation and impairs tumour growth. Nature *552*, 116–120.

Gros, A., Parkhurst, M.R., Tran, E., Pasetto, A., Robbins, P.F., Ilyas, S., Prickett, T.D., Gartner, J.J., Crystal, J.S., Roberts, I.M., et al. (2016). Prospective identification of neoantigen-specific lymphocytes in the peripheral blood of melanoma patients. Nat. Med. *22*, 433–438.

Gubin, M.M., Zhang, X., Schuster, H., Caron, E., Ward, J.P., Noguchi, T., Ivanova, Y., Hundal, J., Arthur, C.D., Krebber, W.J., et al. (2014). Checkpoint blockade cancer immunotherapy targets tumour-specific mutant antigens. Nature *515*, 577–581.

Gubin, M.M., Artyomov, M.N., Mardis, E.R., and Schreiber, R.D. (2015). Tumor neoantigens: building a framework for personalized cancer immunotherapy. J. Clin. Invest. *125*, 3413–3421.

Gubin, M.M., Esaulova, E., Ward, J.P., Malkova, O.N., Runci, D., Wong, P., Noguchi, T., Arthur, C.D., Meng, W., Alspach, E., et al. (2018). High-Dimensional Analysis Delineates Myeloid and Lymphoid Compartment Remodeling during Successful Immune-Checkpoint Cancer Therapy. Cell *175*, 1014–1030.e19.

Guillerey, C., Huntington, N.D., and Smyth, M.J. (2016). Targeting natural killer cells in cancer immunotherapy. Nat. Immunol. *17*, 1025–1036.

Haabeth, O.A.W., Tveita, A.A., Fauskanger, M., Schjesvold, F., Lorvik, K.B., Hofgaard, P.O., Omholt, H., Munthe, L.A., Dembic, Z., Corthay, A., and Bogen, B. (2014). How Do CD4(+) T Cells Detect and Eliminate Tumor Cells That Either Lack or Express MHC Class II Molecules? Front. Immunol. *5*, 174.

Hausser, J., and Strimmer, K. (2009). Entropy Inference and the James-Stein Estimator, with Application to Nonlinear Gene Association Networks. J. Mach. Learn. Res. *10*, 1469–1484.

Hellmann, M.D., Nathanson, T., Rizvi, H., Creelan, B.C., Sanchez-Vega, F., Ahuja, A., Ni, A., Novik, J.B., Mangarin, L.M.B., Abu-Akeel, M., et al. (2018). Genomic Features of Response to Combination Immunotherapy in Patients with Advanced Non-Small-Cell Lung Cancer. Cancer Cell *33*, 843–852.

Hugo, W., Zaretsky, J.M., Sun, L., Song, C., Moreno, B.H., Hu-Lieskovan, S., Berent-Maoz, B., Pang, J., Chmielowski, B., Cherry, G., et al. (2016). Genomic and Transcriptomic Features of Response to Anti-PD-1 Therapy in Metastatic Melanoma. Cell *165*, 35–44.

Ishihama, Y., Rappsilber, J., Andersen, J.S., and Mann, M. (2002). Microcolumns with self-assembled particle frits for proteomics. J. Chromatogr. A *979*, 233–239.

Jamal-Hanjani, M., Wilson, G.A., McGranahan, N., Birkbak, N.J., Watkins, T.B.K., Veeriah, S., Shafi, S., Johnson, D.H., Mitter, R., Rosenthal, R., et al.; TRACERx Consortium (2017). Tracking the Evolution of Non-Small-Cell Lung Cancer. N. Engl. J. Med. *376*, 2109–2121.

Janiszewska, M., Tabassum, D.P., Castaño, Z., Cristea, S., Yamamoto, K.N., Kingston, N.L., Murphy, K.C., Shu, S., Harper, N.W., Del Alcazar, C.G., et al. (2019). Subclonal cooperation drives metastasis by modulating local and systemic immune microenvironments. Nat. Cell Biol. *21*, 879–888.

Kalaora, S., Barnea, E., Merhavi-Shoham, E., Qutob, N., Teer, J.K., Shimony, N., Schachter, J., Rosenberg, S.A., Besser, M.J., Admon, A., and Samuels, Y. (2016). Use of HLA peptidomics and whole exome sequencing to identify human immunogenic neo-antigens. Oncotarget *7*, 5110–5117.

Kalaora, S., Wolf, Y., Feferman, T., Barnea, E., Greenstein, E., Reshef, D., Tirosh, I., Reuben, A., Patkar, S., Levy, R., et al. (2018). Combined Analysis of Antigen Presentation and T-cell Recognition Reveals Restricted Immune Responses in Melanoma. Cancer Discov. *8*, 1366–1375.

Kassambara, A., Kosinski, M., Biecek, P., and Fabian, S. (2017). Package 'survminer'. https://cran.r-project.org/web/packages/survminer/survminer.pdf.

Kather, J.N., Suarez-Carmona, M., Charoentong, P., Weis, C.A., Hirsch, D., Bankhead, P., Horning, M., Ferber, D., Kel, I., Herpel, E., et al. (2018). Topography of cancer-associated immune cells in human solid tumors. eLife *7*, e36967.

König, L., Mairinger, F.D., Hoffmann, O., Bittner, A.K., Schmid, K.W., Kimmig, R., Kasimir-Bauer, S., and Bankfalvi, A. (2019). Dissimilar patterns of tumor-infiltrating immune cells at the invasive tumor front and tumor center are

associated with response to neoadjuvant chemotherapy in primary breast cancer. BMC Cancer *19*, 120.

Krepler, C., Sproesser, K., Brafford, P., Beqiri, M., Garman, B., Xiao, M., Shannan, B., Watters, A., Perego, M., Zhang, G., et al. (2017). A Comprehensive Patient-Derived Xenograft Collection Representing the Heterogeneity of Melanoma. Cell Rep. *21*, 1953–1967.

Kurtulus, S., Madi, A., Escobar, G., Klapholz, M., Nyman, J., Christian, E., Pawlak, M., Dionne, D., Xia, J., Rozenblatt-Rosen, O., et al. (2019). Checkpoint Blockade Immunotherapy Induces Dynamic Changes in PD-1(-)CD8(+) Tumor-Infiltrating T Cells. Immunity *50*, 181–194.e6.

Larkin, J., Chiarion-Sileni, V., Gonzalez, R., Grob, J.J., Cowey, C.L., Lao, C.D., Schadendorf, D., Dummer, R., Smylie, M., Rutkowski, P., et al. (2015). Combined Nivolumab and Ipilimumab or Monotherapy in Untreated Melanoma. N. Engl. J. Med. *373*, 23–34.

Lesur, A., and Domon, B. (2015). Advances in high-resolution accurate mass spectrometry application to targeted proteomics. Proteomics *15*, 880–890.

Li, H., and Durbin, R. (2010). Fast and accurate long-read alignment with Burrows-Wheeler transform. Bioinformatics *26*, 589–595.

Li, H., Handsaker, B., Wysoker, A., Fennell, T., Ruan, J., Homer, N., Marth, G., Abecasis, G., and Durbin, R.; 1000 Genome Project Data Processing Subgroup (2009). The Sequence Alignment/Map format and SAMtools. Bioinformatics *25*, 2078–2079.

Li, H., van der Leun, A.M., Yofe, I., Lubling, Y., Gelbard-Solodkin, D., van Akkooi, A.C.J., van den Braber, M., Rozeman, E.A., Haanen, J., Blank, C.U., et al. (2019). Dysfunctional CD8 T Cells Form a Proliferative, Dynamically Regulated Compartment within Human Melanoma. Cell *176*, 775–789.e18.

Linnemann, C., van Buuren, M.M., Bies, L., Verdegaal, E.M.E., Schotte, R., Calis, J.J.A., Behjati, S., Velds, A., Hilkmann, H., Atmioui, D.E., et al. (2015). High-throughput epitope discovery reveals frequent recognition of neo-antigens by CD4+ T cells in human melanoma. Nat. Med. *21*, 81–85.

Ljunggren, H.G., Stam, N.J., Ohlén, C., Neefjes, J.J., Höglund, P., Heemels, M.T., Bastin, J., Schumacher, T.N., Townsend, A., Kärre, K., et al. (1990). Empty MHC class I molecules come out in the cold. Nature *346*, 476–480.

Lladser, A., Ljungberg, K., Tufvesson, H., Tazzari, M., Roos, A.K., Quest, A.F., and Kiessling, R. (2010). Intradermal DNA electroporation induces survivin-specific CTLs, suppresses angiogenesis and confers protection against mouse melanoma. Cancer Immunol. Immunother. *59*, 81–92.

Lutz, M.B., Kukutsch, N., Ogilvie, A.L., Rossner, S., Koch, F., Romani, N., and Schuler, D. (1999). An advanced culture method for generating large quantities of highly pure dendritic cells from mouse bone marrow. J. Immunological Methods *223*, 77–92.

Marusyk, A., Tabassum, D.P., Altrock, P.M., Almendro, V., Michor, F., and Polyak, K. (2014). Non-cell-autonomous driving of tumour growth supports subclonal heterogeneity. Nature *514*, 54–58.

McDonald, K.A., Kawaguchi, T., Qi, Q., Peng, X., Asaoka, M., Young, J., Opyrchal, M., Yan, L., Patnaik, S., Otsuji, E., and Takabe, K. (2019). Tumor Heterogeneity Correlates with Less Immune Response and Worse Survival in Breast Cancer Patients. Ann. Surg. Oncol. *26*, 2191–2199.

McGranahan, N., and Swanton, C. (2017). Clonal Heterogeneity and Tumor Evolution: Past, Present, and the Future. Cell *168*, 613–628.

McGranahan, N., Furness, A.J., Rosenthal, R., Ramskov, S., Lyngaa, R., Saini, S.K., Jamal-Hanjani, M., Wilson, G.A., Birkbak, N.J., Hiley, C.T., et al. (2016). Clonal neoantigens elicit T cell immunoreactivity and sensitivity to immune checkpoint blockade. Science *351*, 1463–1469.

McKenna, A., Hanna, M., Banks, E., Sivachenko, A., Cibulskis, K., Kernytsky, A., Garimella, K., Altshuler, D., Gabriel, S., Daly, M., and DePristo, M.A. (2010). The Genome Analysis Toolkit: a MapReduce framework for analyzing next-generation DNA sequencing data. Genome Res. *20*, 1297–1303.

Miao, D., Margolis, C.A., Gao, W., Voss, M.H., Li, W., Martini, D.J., Norton, C., Bossé, D., Wankowicz, S.M., Cullen, D., et al. (2018a). Genomic correlates of response to immune checkpoint therapies in clear cell renal cell carcinoma. Science *359*, 801–806.

Miao, D., Margolis, C.A., Vokes, N.I., Liu, D., Taylor-Weiner, A., Wankowicz, S.M., Adeegbe, D., Keliher, D., Schilling, B., Tracy, A., et al. (2018b). Genomic correlates of response to immune checkpoint blockade in microsatellite-stable solid tumors. Nat. Genet. *50*, 1271–1281.

Miller, C.A., White, B.S., Dees, N.D., Griffith, M., Welch, J.S., Griffith, O.L., Vij, R., Tomasson, M.H., Graubert, T.A., Walter, M.J., et al. (2014). SciClone: inferring clonal architecture and tracking the spatial and temporal patterns of tumor evolution. PLoS Comput. Biol. *10*, e1003665.

Milner, E., Gutter-Kapon, L., Bassani-Strenberg, M., Barnea, E., Beer, I., and Admon, A. (2013). The effect of proteasome inhibition on the generation of the human leukocyte antigen (HLA) peptidome. Mol. Cell. Proteomics *12*, 1853–1864.

Milo, I., Bedora-Faure, M., Garcia, Z., Thibaut, R., Périé, L., Shakhar, G., Deriano, L., and Bousso, P. (2018). The immune system profoundly restricts intra-tumor genetic heterogeneity. Sci. Immunol. *3*, eaat1435.

Morris, L.G., Riaz, N., Desrichard, A., Şenbabaoğlu, Y., Hakimi, A.A., Makarov, V., Reis-Filho, J.S., and Chan, T.A. (2016). Pan-cancer analysis of intratumor heterogeneity as a prognostic determinant of survival. Oncotarget *7*, 10051–10063.

Muranski, P., Boni, A., Antony, P.A., Cassard, L., Irvine, K.R., Kaiser, A., Paulos, C.M., Palmer, D.C., Touloukian, C.E., Ptak, K., et al. (2008). Tumor-specific Th17-polarized cells eradicate large established melanoma. Blood *112*, 362–373.

Newman, A.M., Liu, C.L., Green, M.R., Gentles, A.J., Feng, W., Xu, Y., Hoang, C.D., Diehn, M., and Alizadeh, A.A. (2015). Robust enumeration of cell subsets from tissue expression profiles. Nat. Methods *12*, 453–457.

Nielsen, M., Lundegaard, C., Worning, P., Lauemøller, S.L., Lamberth, K., Buus, S., Brunak, S., and Lund, O. (2003). Reliable prediction of T-cell epitopes using neural networks with novel sequence representations. Protein Sci. *12*, 1007–1017.

Olshen, A.B., Venkatraman, E.S., Lucito, R., and Wigler, M. (2004). Circular binary segmentation for the analysis of array-based DNA copy number data. Biostatistics *5*, 557–572.

Patel, S.J., Sanjana, N.E., Kishton, R.J., Eidizadeh, A., Vodnala, S.K., Cam, M., Gartner, J.J., Jia, L., Steinberg, S.M., Yamamoto, T.N., et al. (2017). Identification of essential genes for cancer immunotherapy. Nature *548*, 537–542.

Patro, R., Duggal, G., Love, M.I., Irizarry, R.A., and Kingsford, C. (2017). Salmon provides fast and bias-aware quantification of transcript expression. Nat. Methods *14*, 417–419.

Porgador, A., Brenner, B., Vadai, E., Feldman, M., and Eisenbach, L. (1991). Immunization by gamma-IFN-treated B16-F10.9 melanoma cells protects against metastatic spread of the parental tumor. Int. J. Cancer Suppl. *6*, 54–60.

Quezada, S.A., Simpson, T.R., Peggs, K.S., Merghoub, T., Vider, J., Fan, X., Blasberg, R., Yagita, H., Muranski, P., Antony, P.A., et al. (2010). Tumor-reactive CD4(+) T cells develop cytotoxic activity and eradicate large established melanoma after transfer into lymphopenic hosts. J. Exp. Med. *207*, 637–650.

Rappsilber, J., Ishihama, Y., and Mann, M. (2003). Stop and go extraction tips for matrix-assisted laser desorption/ionization, nanoelectrospray, and LC/MS sample pretreatment in proteomics. Anal. Chem. *753*, 663–670.

Reuben, A., Spencer, C.N., Prieto, P.A., Gopalakrishnan, V., Reddy, S.M., Miller, J.P., Mao, X., De Macedo, M.P., Chen, J., Song, X., et al. (2017). Genomic and immune heterogeneity are associated with differential responses to therapy in melanoma. NPJ Genom. Med. *2*, 10.

Riaz, N., Havel, J.J., Makarov, V., Desrichard, A., Urba, W.J., Sims, J.S., Hodi, F.S., Martin-Algarra, S., Mandal, R., Sharfman, W.H., et al. (2017). Tumor and Microenvironment Evolution during Immunotherapy with Nivolumab. Cell *171*, 934–949.e16.

Ribas, A., and Wolchok, J.D. (2018). Cancer immunotherapy using checkpoint blockade. Science *359*, 1350–1355.

Rizvi, N.A., Hellmann, M.D., Snyder, A., Kvistborg, P., Makarov, V., Havel, J.J., Lee, W., Yuan, J., Wong, P., Ho, T.S., et al. (2015). Cancer immunology. Mutational landscape determines sensitivity to PD-1 blockade in non-small cell lung cancer. Science *348*, 124–128.

Rollman, E., Smith, M.Z., Brooks, A.G., Purcell, D.F., Zuber, B., Ramshaw, I.A., and Kent, S.J. (2007). Killing kinetics of simian immunodeficiency virus-specific CD8+ T cells: implications for HIV vaccine strategies. J. Immunol. *179*, 4571–4579.

Rooney, M.S., Shukla, S.A., Wu, C.J., Getz, G., and Hacohen, N. (2015). Molecular and genetic properties of tumors associated with local immune cytolytic activity. Cell *160*, 48–61.

Rosenthal, R., McGranahan, N., Herrero, J., Taylor, B.S., and Swanton, C. (2016). DeconstructSigs: delineating mutational processes in single tumors distinguishes DNA repair deficiencies and patterns of carcinoma evolution. Genome Biol. *17*, 31.

Rosenthal, R., Cadieux, E.L., Salgado, R., Bakir, M.A., Moore, D.A., Hiley, C.T., Lund, T., Tanić, M., Reading, J.L., Joshi, K., et al.; TRACERx consortium (2019). Neoantigen-directed immune escape in lung cancer evolution. Nature *567*, 479–485.

Sade-Feldman, M., Yizhak, K., Bjorgaard, S.L., Ray, J.P., de Boer, C.G., Jenkins, R.W., Lieb, D.J., Chen, J.H., Frederick, D.T., Barzily-Rokni, M., et al. (2018). Defining T Cell States Associated with Response to Checkpoint Immunotherapy in Melanoma. Cell *175*, 998–1013.e20.

Sahin, U., and Türeci, Ö. (2018). Personalized vaccines for cancer immunotherapy. Science *359*, 1355–1360.

Samstein, R.M., Lee, C.-H., Shoushtari, A.N., Hellmann, M.D., Shen, R., Janjigian, Y.Y., Barron, D.A., Zehir, A., Jordan, E.J., Omuro, A., et al. (2019). Tumor mutational load predicts survival after immunotherapy across multiple cancer types. Nat. Genet. *51*, 202–206.

Schindelin, J., Arganda-Carreras, I., Frise, E., Kaynig, V., Longair, M., Pietzsch, T., Preibisch, S., Rueden, C., Saalfeld, S., Schmid, B., et al. (2012). Fiji: an open-source platform for biological-image analysis. Nat. Methods *9*, 676–682.

Sharma, P., Hu-Lieskovan, S., Wargo, J.A., and Ribas, A. (2017). Primary, Adaptive, and Acquired Resistance to Cancer Immunotherapy. Cell *168*, 707–723.

Shi, T., Song, E., Nie, S., Rodland, K.D., Liu, T., Qian, W.J., and Smith, R.D. (2016). Advances in targeted proteomics and applications to biomedical research. Proteomics *16*, 2160–2182.

Shi, W., Ng, C.K.Y., Lim, R.S., Jiang, T., Kumar, S., Li, X., Wali, V.B., Piscuoglio, S., Gerstein, M.B., Chagpar, A.B., et al. (2018). Reliability of Whole-Exome Sequencing for Assessing Intratumor Genetic Heterogeneity. Cell Rep. *25*, 1446–1457.

Snyder, A., Makarov, V., Merghoub, T., Yuan, J., Zaretsky, J.M., Desrichard, A., Walsh, L.A., Postow, M.A., Wong, P., Ho, T.S., et al. (2014). Genetic basis for clinical response to CTLA-4 blockade in melanoma. N. Engl. J. Med. *371*, 2189–2199.

Spranger, S. (2016). Tumor Heterogeneity and Tumor Immunity: A Chicken-and-Egg Problem. Trends Immunol. *37*, 349–351.

Spranger, S., Luke, J.J., Bao, R., Zha, Y., Hernandez, K.M., Li, Y., Gajewski, A.P., Andrade, J., and Gajewski, T.F. (2016). Density of immunogenic antigens does not explain the presence or absence of the T-cell-inflamed tumor microenvironment in melanoma. Proc. Natl. Acad. Sci. USA *113*, E7759–E7768.

Strønen, E., Toebes, M., Kelderman, S., van Buuren, M.M., Yang, W., van Rooij, N., Donia, M., Böschen, M.L., Lund-Johansen, F., Olweus, J., and Schumacher, T.N. (2016). Targeting of cancer neoantigens with donor-derived T cell receptor repertoires. Science *352*, 1337–1341.

Talevich, E., Shain, A.H., Botton, T., and Bastian, B.C. (2016). CNVkit: Genome-Wide Copy Number Detection and Visualization from Targeted DNA Sequencing. PLoS Comput. Biol. *12*, e1004873.

Tanaka, A., and Sakaguchi, S. (2017). Regulatory T cells in cancer immunotherapy. Cell Res. *27*, 109–118.

Therneau, T.M., and Grambsch, P.M. (2000). Modeling Survival Data: Extending the Cox Model (New York: Springer-Verlag).

Tran, E., Turcotte, S., Gros, A., Robbins, P.F., Lu, Y.-C., Dudley, M.E., Wunderlich, J.R., Somerville, R.P., Hogan, K., Hinrichs, C.S., et al. (2014). Cancer immunotherapy based on mutation-specific CD4+ T cells in a patient with epithelial cancer. Science *344*, 641–645.

Van Allen, E.M., Miao, D., Schilling, B., Shukla, S.A., Blank, C., Zimmer, L., Sucker, A., Hillen, U., Foppen, M.H.G., Goldinger, S.M., et al. (2015). Genomic correlates of response to CTLA-4 blockade in metastatic melanoma. Science *350*, 207–211.

Veatch, J.R., Lee, S.M., Fitzgibbon, M., Chow, I.T., Jesernig, B., Schmitt, T., Kong, Y.Y., Kargl, J., Houghton, A.M., Thompson, J.A., et al. (2018). Tumor-infiltrating BRAFV600E-specific CD4+ T cells correlated with complete clinical response in melanoma. J. Clin. Invest. *128*, 1563–1568.

Viros, A., Sanchez-Laorden, B., Pedersen, M., Furney, S.J., Rae, J., Hogan, K., Ejiama, S., Girotti, M.R., Cook, M., Dhomen, N., and Marais, R. (2014). Ultraviolet radiation accelerates BRAF-driven melanomagenesis by targeting TP53. Nature *511*, 478–482.

Wang, J., Perry, C.J., Meeth, K., Thakral, D., Damsky, W., Micevic, G., Kaech, S., Blenman, K., and Bosenberg, M. (2017). UV-induced somatic mutations elicit a functional T cell response in the YUMMER1.7 mouse melanoma model. Pigment Cell Melanoma Res. *30*, 428–435.

Williams, M.J., Werner, B., Barnes, C.P., Graham, T.A., and Sottoriva, A. (2016). Identification of neutral tumor evolution across cancer types. Nat. Genet. *48*, 238–244.

Wolf, Y., and Samuels, Y. (2018). Cancer research in the era of immunogenomics. ESMO Open *3*, e000475.

Wolf, Y., Shemer, A., Levy-Efrati, L., Gross, M., Kim, J.S., Engel, A., David, E., Chappell-Maor, L., Grozovski, J., Rotkopf, R., et al. (2018). Microglial MHC class II is dispensable for experimental autoimmune encephalomyelitis and cuprizone-induced demyelination. Eur. J. Immunol. *48*, 1308–1318.

Zanetti, M. (2015). Tapping CD4 T cells for cancer immunotherapy: the choice of personalized genomics. J. Immunol. *194*, 2049–2056.

STAR★METHODS

KEY RESOURCES TABLE

REAGENT or RESOURCE	SOURCE	IDENTIFIER
Antibodies		
anti-p53 (1C12) Mouse mAb	Cell signaling	Cat#2524; RRID:AB_331743
Mouse anti-GAPDH	Millipore	Clone 6C5 Cat#MAB374; RRID:AB_2107445
Peroxidase Affinipure Goat anti-Mouse IgG	Jackson ImmunoResearch Labs	Cat#115-035-003; RRID:AB_10015289
anti-mouse PD-1 (CD279)	BioXCell	29F.1.A12 Cat#: BE0273; RRID: AB_2687796
Rat IgG2a isotype control	BioXCell	2A3, Cat#: BE0089; RRID: AB_1107769
Alexa Fluor700 anti-mouse CD45	Biolegend	Clone 30-F11 Cat#103128; RRID:AB_493715
PerCP/Cy5.5 anti-mouse CD8a	Biolegend	clone 53-6.7 Cat#100734; RRID:AB_2075238
APC/Cy7 anti-mouse CD4	Biolegend	clone GK1.5 Cat#100413; RRID:AB_312698
FITC anti- mouse CD107a (LAMP-1)	Biolegend	clone 1D4B Cat#121605; RRID:AB_572006
Pacific Blue anti-Granzyme B	Biolegend	clone GB11 Cat#515407; RRID:AB_2562195
PE/Cy7 anti- mouse IFN-γ	Biolegend	clone XMG12 Cat #505826; RRID:AB_2295770
Pacific Blue anti-mouse CD8a	Biolegend	Clone 53-6.7 Cat#100728; RRID:AB_493426
PerCP anti-mouse CD4	Biolegend	clone GK1.5 Cat#100431; RRID:AB_893329
FITC anti-mouse CD45	Biolegend	Clone 30-F11 Cat#103108; RRID:AB_312973
PE/Cy7 anti-mouseCD90.2 (Thy-1.2)	Biolegend	Clone 30-H12 Cat#105325; RRID:AB_2303142
PE anti-mouseTCRβ	Biolegend	clone H57-597 Cat#109207; RRID:AB_313430
a-CD8a rat monoclonal antibody	eBioscience	Clone 4SM15 Cat#14-0808-82; RRID:AB_2572861
Biotin Donkey anti Rat IgG (H+L)	Jackson ImmunoResearch	Cat#712-065-153; RRID:AB_2315779
anti-CD3 rabbit monoclonal antibody [SP7]	Abcam	Cat#ab16669; RRID:AB_443425
anti-FoxP3 rat monoclonal antibody (FJK-16 s)	Thermo Fisher Scientific	Cat#14-5773-82; RRID:AB_467576
Cy2 Donkey anti Rabbit IgG (H+L)	Jackson ImmunoResearch	Cat#711-225-152; RRID:AB_2340612
Cy3 Donkey anti Rat IgG (H+L)	Jackson ImmunoResearch	Cat#712-165-153; RRID:AB_2340667
anti-CPD	Cosmo Bio	Cat#CAC-NM-DND-001; RRID:AB_1962813
Cy3 Donkey anti Mouse IgG (H+L)	Jackson ImmunoResearch	Cat#715-165-151; RRID:AB_2315777
anti-H2-Kb	ATCC	Cat#20-8-4 s (HB-11)
anti-H2-Db	In house; generated from hybridoma purchased from ATCC	Cat#28-14-8 s (HB-27)
APC anti-mouse H-2Kb	In house; generated from hybridoma purchased from ATCC	clone AF6-88.5 Cat#116517; RRID:AB_10568693
PE anti-mouse H-2Db	BioLegend	clone KH95 Cat#111507; RRID:AB_313512
APC anti-CD11c	Thermo Fisher Scientific	Clone N418 Cat# 17-0114-81; RRID:AB_469345
Pacific Blue(TM) anti-mouse CD80 antibody	BioLegend	Clone 16-10A1 Cat# 104723; RRID:AB_2076001
PE Anti-Mouse CD86 (B7-2)	Thermo Fisher Scientific	Clone PO3.1 Cat# 12-0861-81; RRID:AB_465764
PE/Cy7 anti-mouse I-Ab (Anti-MHCII)	BioLegend	Clone AF6-120.1 Cat# 116419; RRID:AB_10575904
PerCP-Cyanine5.5 CD197 (CCR7) Monoclonal Antibody (4B12)	Thermo Fisher Scientific	Clone 4B12 Cat# 45-1971-80; RRID:AB_925738
APC Anti-Mouse CD45.1	Thermo Fisher Scientific	Clone A20 Cat# 17-0453-82; RRID:AB_469398
Chemicals, Peptides, and Recombinant Proteins		
RPMI	Biological Industries	Cat#01-100-1A
FBS	GIBCO	Cat#12657-029

Continued

REAGENT or RESOURCE	SOURCE	IDENTIFIER
L-glutamine	Biological Industries	Cat#03-020-1B
Penicillin/Streptomycin antibiotics	Invitrogen	Cat#15140163
HEPES	Sigma	Cat#H0887
DMEM	GIBCO	Cat#41965-039
MCDB 153	Sigma	Cat# M7403
L-15 Medium (Leibovitz)	Sigma	Cat#L1518
bovine insulin	Sigma	Cat#I0516
SDS Solution 20%	Bio-Rad	Cat# 161-0418
SYBR Green I	Invitrogen	Cat#S7567
Water, ultra-pure	Biological Industries	Cat#01-866-1A
β-mercaptoethanol	EMD Millipore Corp.	Cat#444203
Dulbecco's Phosphate Buffered Saline (PBS)	Biological Industries	Cat#02-023-1A
sodium pyruvate	Biological Industries	Cat#03-042-1B
MEM-Eagle Non-essential amino acids solution	Biological Industries	Cat#01-340-1B
Recombinant Mouse Granulocyte Macrophage Colony Stimulating Factor GM-CSF Mouse	PROSPEC	Cat#cyt-222
Lipopolysaccharides (LPS) from E-coli	Sigma	Cat#L26630
Opti-MEM Reduced Serum Medium	GIBCO	Cat#31985-047
CFSE	eBioscience	Cat#65-0850-84
Collagenase D	Roche	Cat# 11088866001
DNase I	Roche	Cat#10104159001
BSA	Sigma	Cat# A9418
HBSS (w/o Ca^{2+} or Mg++)	Bio-Lab	Cat#004717237500
Collagenase IV	gibco	Cat#17104-019
EGTA	Merck	Cat# 324626.25
polyvinyl alcohol (PVA)	Sigma	Cat# P8136
trypsin	Sigma	Cat# T4549
Optiprep	Sigma	Cat#D1556
Versen	Lonza	Cat#17-711E
Paraformaldehyde (PFA)	Electron Microscopy Sciences	Cat#15710
hematoxylin	Sigma	Cat#GHS316
Hoechst	Invitrogen	Cat#LSH3570
Protease Inhibitors Cocktail	Sigma	Cat#P8340
sodium deoxycholate	Sigma	Cat#D6750
iodoacetamide	Sigma	Cat#I6125
EDTA	Promega	Cat#V4231
PMSF	Sigma	Cat#78830
octyl-β-D glucopyranoside	Sigma	Cat#O8001
Protein-A Resin	A₂S	Cat#L00210
FAIFNTEQM synthetic peptide	GenScript Biotech Corp.	N/A
VINENYDYL synthetic peptide	GenScript Biotech Corp.	N/A
SAYEKLYSL synthetic peptide	GenScript Biotech Corp.	N/A
ASLTHVDSL synthetic peptide	GenScript Biotech Corp.	N/A
LANETISTL synthetic peptide	GenScript Biotech Corp.	N/A
VAHIFVIGV synthetic peptide	GenScript Biotech Corp.	N/A
AGLLNSPHFI synthetic peptide	GenScript Biotech Corp.	N/A
HQNVNVENI synthetic peptide	GenScript Biotech Corp.	N/A
QAFDFAYV synthetic peptide	GenScript Biotech Corp.	N/A

Continued

REAGENT or RESOURCE	SOURCE	IDENTIFIER
FAALLRYSI synthetic peptide	GenScript Biotech Corp.	N/A
SMYLVSKL synthetic peptide	GenScript Biotech Corp.	N/A
Critical Commercial Assays		
BD Cytofix/Cytoperm Kit	Thermo Fisher Scientific	Cat#BD 554714
SENSE Total RNA-Seq Library Prep Kit for Illumina),	Lexogen	Cat#LX-009.96 1
DNeasy Blood & Tissue Kit	QIAGEN	Cat# 69504
SureSelectXT Mouse All Exon System	Agilent Technologies	Cat# 5190-4641
Dynabeads mRNA DIRECT Kit	Invitrogen	Cat#61012
SuperSignal WestPicoPLUS Chemiluminescent Suibstrat	Thermo Fisher Scientific	Cat#34580
3,3′-Diaminobenzidine tetrahydrochloride	Sigma	Cat# D5905
Deposited Data		
Mouse WES sequencing data	This paper	https://www.ebi.ac.uk/ena; accession number: PRJEB25961, secondary accession: ERP107928.
Mouse CD8$^+$ T cell RNaseq data	This paper	https://github.com/bioinf-dev/Wolf_et_al_Cell_2019/blob/master/Other/RNAseq_mouse_CD8Tcell_TPM.txt
Processed data and code used for Figures 1, 2, 3, and 7	This paper (Figures 1, 2, and 3). For Figure 7 Snyder et al., 2014; Riaz et al., 2017; Hugo et al., 2016; and Van Allen et al., 2015	https://github.com/bioinf-dev/Wolf_et_al_Cell_2019
MS spectra of the identified neoantigenes and synthetic peptides	This paper	https://github.com/bioinf-dev/Wolf_et_al_Cell_2019/blob/master/Other/Spectra.pdf
Experimental Models: Cell Lines		
Murine melanoma B2905	Laboratory of Prof. Merlino	N/A
B16F10.9	Laboratory of Prof. Eisenbach	N/A
RMA-s	Laboratory of Prof. Eisenbach	RRID:CVCL_2180
Experimental Models: Organisms/Strains		
C57BL/6JOlaHst	Envigo	N/A
NOD.*Cg-Prkdc*^{scid}*Il2rg*^{tm1Wjl}/SzJ (NSG)	The Jackson Laboratory	Cat#JAX:005557 RRID:IMSR_JAX:005557
B6.129S4-*Cd80*^{tm1Shr} *Cd86*^{tm2Shr}/J (CD80/86 −/− Double KO)	Laboratory of Prof. Jung	Cat# JAX:003610 RRID:IMSR_JAX:003610
Software and Algorithms		
FlowJo software	Tree Star	N/A
Prism	GraphPad	N/A
ImageLab 5.1 software	BioRad	N/A
FIJI	ImageJ	Schindelin et al., 2012
CHAT v1.0	Snyder et al., 2014	https://cran.r-project.org/src/contrib/Archive/CHAT/
deconstructSigs v1.8.0	Rosenthal et al., 2016	https://www.rdocumentation.org/packages/deconstructSigs/versions/1.8.0
NetMHC v4.0	Nielsen et al., 2003	http://www.cbs.dtu.dk/services/NetMHC/
SciClone v1.1.0	Miller et al., 2014	https://www.rdocumentation.org/packages/sciClone/versions/1.1.0/topics/sciClone
Maxqaunt v1.5.3.8	Cox and Mann, 2008	http://coxdocs.org/doku.php?id=maxquant:start
samtools v1.8	Li et al., 2009	http://www.htslib.org/

(Continued on next page)

Continued

REAGENT or RESOURCE	SOURCE	IDENTIFIER
Trimomatic v0.36	Bolger et al., 2014	http://www.usadellab.org/cms/index.php?page=trimmomatic
Salmon v0.9.2	Patro et al., 2017	https://salmon.readthedocs.io/en/latest/building.html
GATK v3.6	McKenna et al., 2010	https://software.broadinstitute.org/gatk/
CNVkit	Talevich et al., 2016	https://cnvkit.readthedocs.io/en/stable/
CloneEvol	Talevich et al., 2016	https://github.com/hdng/clonevol
BWA	Li and Durbin, 2010	http://bio-bwa.sourceforge.net/
vcf2maf	N/A	https://github.com/mskcc/vcf2maf
bcftools v1.3	Li et al., 2009	https://github.com/samtools/bcftools
Rstudio v1.1.423	N/A	https://www.rstudio.com/products/rstudio/
R 'survival' package v2.43-3.	Therneau and Grambsch, 2000	https://cran.r-project.org/web/packages/survival/index.html
R 'entropy' package v1.2.1	Hausser and Strimmer, 2009	https://cran.r-project.org/web/packages/entropy/index.html
R 'ggsurvplot' function	Kassambara et al., 2017	https://cran.r-project.org/web/packages/survminer/index.html

LEAD CONTACT AND MATERIALS AVAILABILITY

Further information and requests for resources and reagents should be directed to and will be fulfilled by the Lead Contact, Yardena Samuels, (Yardena.Samuels@weizmann.ac.il)

There are restrictions to the availability of the B2905 cell as they require an MTA.

EXPERIMENTAL MODEL AND SUBJECT DETAILS

Mice

Animals were maintained in a specific pathogen-free (SPF), temperature-controlled (22°C ± 1°C) mouse facility on a reverse 12-hour light, 12-hour dark cycle at the Weizmann Institute of Science. Food and water were given *ad libitum*. Mice were handled under protocols approved by the Weizmann Institute Animal Care Committee (IACUC 11440219-2) in accordance with international guidelines.

To generate syngeneic mouse cancer models, 6 weeks old female C57BL/6 (purchased from Envigo), NSG (The Jackson Laboratory) and CD80/86 $^{-/-}$ (kindly provided by Prof Steffen Jung, The Weizmann Institute) were used.

Cell lines

Murine melanoma B2905, derived from a UV-irradiated HGF-transgenic mouse on a C57BL/6 background (Patel et al., 2017) and B16F10.9 (Porgador et al., 1991) were used. The B2905 cell line was grown in RPMI (Biological Industries) containing 10% heat inactivated FBS (GIBCO), 1% L-glutamine (Biological Industries), 1% Penicillin/Streptomycin antibiotics (Invitrogen) and 12.5mM HEPES (Sigma) buffer. B16F10.9 cells were grown in DMEM medium (GIBCO) containing 10% heat inactivated FBS, 1% L-glutamine, 1% Penicillin/Streptomycin antibiotics. Both cell lines originated from male mice. Primary cell lines that were generated from solid tumors, derived from UVB-B2905 as described below, were grown in Tu2% media [80% MCDB 153 (Sigma), 20% Leibovitz's L-15 (Sigma), 5 μg/mL bovine insulin (Sigma), 2% FBS (GIBCO), and 1.68 mM CaCl$_2$]. The murine lymphoma mutant cell line RMA-s (Ljunggren et al., 1990) were cultured in RPMI medium supplemented with 10% heat-inactivated FBS, 40 μg/ml gentamycin sulfate and $5x10^{-5}$M β-mercaptoethanol. All cells were cultured using standard procedures in a 37°C humidified incubator with 5% CO$_2$. Cells were tested routinely for Mycoplasma using Mycoplasma EZ-PCR test kit (cat#20-700-20, Biological Industries).

METHOD DETAILS

UVB exposure

Cells were seeded in 10cm plates. 24 hours later, at confluence of 80%, the cells were exposed to UVB using bench XX-15M 302nm UV lamp. Irradiation was measured using the UVX radiometer (Ultra Violet Products, Cambridge, UK). All cell lines indicated in the study (B2905-UVB, B2905-UVB.2, B16F10.9-UVB) were UVB irradiated with 600J/m2, with the exception of the B2905-UVB.3 cell line, that was sequentially irradiated with 250 J/m^2 for 3 times before isolating and culturing single cell clones from the surviving population.

In vitro proliferation

For *in vitro* proliferation assays, cells were seeded in six replicates (500 cells per well) in 96 well plates and incubated for five to eight days. Samples were analyzed every 24-48 hours by lysing the cells in 50 μL 0.2% SDS/well and incubating at 37°C for 30 minutes. Following incubation, 150 μl/well of SYBR staining solution [1:750 SYBR Green I (Invitrogen), diluted in water] were added and the plates were incubated at room temterature in the dark for ten minutes. Fluorescence intensities were measured for each well using FLUOstar OPTIMA BMG LABTECH reader.

Generation of single-cell clones

For SCCs generation, cells were plated in 96 well plates, in a concentration of 1 cell/well. 10 days later, cells were monitored and wells that showed more than one focal clone were excluded. Single clones were passaged to establish cell lines. The number of passages was controlled.

Western blotting

24 hours post irradiation, cells were washed once with PBS and scraped and harvested in sample buffer (2.5% w/v SDS, 25% v/v Glycerol, 125mM Tris pH-6.8, 0.01% w/v bromophenol blue, 4% β-mercaptoethanol, in water). Samples were sonicated for ten seconds (30% amplitude, Branson Digital Sonifier) and heated at 95°C for 5 minutes. Proteins were resolved on 10% SDS-polyacrilamide gels and transferred to 0.45μm nitrocellulose membranes (Bio-Rad). Western blots were probed with anti-mouse p53 (Cell signaling) and GAPDH (Millipore). Antibodies were detected using peroxidase-conjugated AffiniPure goat anti-mouse IgG (Jackson ImmunoResearch Labs) and enhanced chemiluminescence western blotting detection reagents (Thermo Fisher scientific). Gels were Imaged by CemiDoc XRS+ (Bio-Rad) and analyzed by ImageLab 5.1 software (BioRad).

In vivo mouse experiments

Tumor inoculation

For experiments with the B2905 cell line, $5*10^5$ cells were injected in 100ul PBS, intradermal, into the right lower flank after shaving. In experiments in which the genomic clonal structure was monitored over time, the same cell line and the same amount of cells ($1*10^5$) were inoculated at the same time, to multiple WT C57B/6 mice. At indicated times post inoculation, tumors were excised (2 mice each time point) and their gDNA was subjected to WES. In experiments in which several clones were inoculated as a mixture, and more than one possible clone could be chosen, we used clones that have similar *in vitro* growth to avoid a large number of passages prior to inoculation. Each clone was equally represented in the mixture, and the total number of injected cells was $5*10^5$. For experiments with the B16F10.9 cell line, $1*10^5$ cells were injected. Tumors were measured using calipers. Tumor volume was assessed by measuring tumor diameter and calculation using the equation $\pi/6*$(tumor diameter)^3. Mice with tumor volume of ≥ 1 cm^3 were euthanized.

Anti PD-1 treatment

anti-PD-1 (29F.1.A12, BioXCell, 250ug) and IgG2a control (2A3, BioXCell, 250ug) antibodies were administrated via retro-orbital injections at days 6,9, and 12 from tumor cells inoculation.

In Vivo *killing assay*

DCs were generated *in vitro* according to Lutz et al. (1999): Femurs and tibiae of 6 weeks old female C57BL/6 mice were removed and purified from the surrounding muscle tissue. Both bone ends were cut with scissors and the marrow was flushed with PBS using a $27^{G1/2}$ Syringe. Clusters within the marrow suspension were disintegrated by vigorous pipetting. Cells were washed with PBS, seeded at 4×10^6 per 100mm bacteriological Petri dishes (Falcon, #351029), in 10 mL DC medium [RPMI, 10% FBS, 1mM sodium pyruvate, x1 non-essential amino acid, 2mM glutamine, 1% Penicillin/Streptomycin antibiotics and $5*10^{-5}$M β-mercaptoethanol] containing 200 U/ml rmGM-CSF (ProSpec), and incubated at 37°C, 5% CO$_2$. Three day later (day 3), additional 10 mL of DC medium containing 200 U/ml rmGM-CSF were added to the plates. At day 6, half of the culture supernatant was collected, centrifuged, and the cell pellet was resuspended in 10 mL fresh DC medium containing 200 U/ml rmGM-CSF, and plated back into the original plate. At day 8, non-adherent cells were harvested, counted, adjusted to $15*10^6$ cells per 10 mL DC medium supplemented with 100U/ml rmGM-CSF and seeded in 10cm plates. At day 9, lipopolysacchride (LPS, Sigma) was added at 1 μg/ml to mature the DCs. At day 10, the cells were collected and washed twice with PBS (1000rpm, 10 min, 18°C). A small fraction of the cells were subjected to FACS analysis, to validate DCs markers: CD11c$^+$CD80$^+$CD86$^+$MHCII$^+$CCR7$^+$. The rest of the DC enriched cell population was adjusted to $6*10^6$ /ml in OptiMEM (GIBCO), and loaded with 50μM synthetic peptide for 3 hours in 37°C. After incubation, cells were washed with PBS and injected *i.p.* to C57BL/6 WT mice (10^6 cell/mouse) in 3 boosts, 7 days apart. 10 days following the last vaccination, splenocytes were isolated from WT CD45.1$^+$ mice that were pulsed with 25μM WT peptide, or left untreated, or loaded with 25uM mutated peptide for 1.5h at 37°C. Following incubation, cells were labeled with 0.03μM or 0.3μM or 3μM CFSE (eBioscience), respectively). A 1:1:1 mixture of the cells (total of 20×10^6) was intravenously transferred to immunized mice and to naive, age matched, control mice. 24 hours later, spleens were excised, stained with anti CD45.1mAb (Thermo Fisher Scientific)

and the differential clearance of the stained cell populations was evaluated using flow cytometry. Stained cells were acquired on LSRII flow cytometer at the Weizmann FACS facility and analyzed using FlowJo software (Tree Star). Specific killing was defined as:

$$\left[1 - \left(\frac{\%\ of\ mut\ peptide\ loaded\ cells\ from\ immunized\ mice}{\%\ of\ unloaded\ cells\ from\ immunized\ mice} \Big/ \frac{\%\ of\ mut\ peptide\ loaded\ cells\ from\ naive\ mice}{\%\ of\ unloaded\ cells\ from\ naive\ mice}\right)\right] * 100$$

Flow cytometry of TILs

Tumors were surgically removed from animals and were place in cold PBS. Following, tumors were mechanically shredded using scalpel and incubated in RPMI medium containing 2mg/ml Collagenase D (Roche), and 2 mg/ml DNaseI (Roche) in 37°C for 20min. The resulting cell suspension was washed with PBS, passed through a 70-μm filter (Falcon) and cells were incubated in FACS buffer (PBS supplemented with 1%BSA (Sigma), 2mM EDTA and 0.05% sodium azide) in the presence of staining antibody. For intracellular staining, the Cytofix/Cytoperm Kit (Fisher Scientific) was used according to the manufacturer's instruction. Cells were acquired on FACSCanto, LSRII, and LSRFortessa systems (BD) and analyzed with FlowJo software (Tree Star). Antibodies used for flow cytometry were: anti-mouse CD8, CD4, TCRβ, CD107a, Granzyme B, and IFN-γ (all Biolegend).

RNA-sequencing

CD45$^+$, Thy-1.2$^+$, TCRβ^+, CD8$^+$ cells were sorted from tumors at day 16 post inoculation using FACSAria II sorter (BD). mRNA was purified from the sorted cells using Dynabeads mRNA DIRECT Purification Kit (Invitrogen), according to the manufactures protocol. RNA-Libraries were constructed using SENSE Total RNA-Seq Library Prep Kit for Illumina (LEXOGEN), loaded onto Illumina NextSeq 500 sequencer using the Nextseq High Output V2 150 sequencing kit (Illumina, 150 bp, single reads).

Secondary cell line generation, derived from UVB-B2905 solid tumors

B2905 cells (5*10^5) were intradermally injected to C57B/6 WT mice. At day 14 post inoculation, fresh tumors were removed and placed on ice in 1X HBSS (w/o Ca^{2+} or Mg++, Bio-Lab, cat #004717237500). Tissues were dissociated according to M. Herlyn's laboratory protocol (Krepler et al., 2017): First, tissues were minced using a cross blade and the slurry was weighted and centrifuged (220 g, 4 min, 4°C). The chopped tissues were resuspended in 10mL of warmed digest media [Collagenase IV (2,000 u/mL, gibco, cat#17104-019), 1M CaCl$_2$, DNase I (10,000 u/mL, Roche, cat#10104159001) in HBSS] per 1g of tumor tissue, and placed in 37°C water bath. 20 min later, samples were washed with HBSS up to 50mL and centrifuged at 220 g, 4 min, 4°C. 1X TEG buffer [To make 1X TEG buffer, first, 10X TEG buffer was prepared as follows: 40mg of EGTA (ethylene glycol bis(2-aminoethyl ether)-N,N,N'N'-tetraacetic acid, Merck) and 10mg of PVA (polyvinyl alcohol, Sigma) were dissolved in 90 mL of warmed 1X PBS. 10 mL of 2.5% trypsin (Sigma) were added and pH was adjusted to pH = 7.4. This 10XfTEG buffer was diluted 1:10 in HBSS] was added at 5mL per 1g tissue, and placed at 37°C for 2 min, followed by the addition of an equal volume of cold staining media [568 mg BSA (Sigma), 57 mL H$_2$O (Biological Industries), 5.7 mL 1M HEPES pH 7.4 (Sigma), 5.7 mL 100x PenStrep (Invitrogen) in 500 mL Leibovitz's L15 media (Invitrogen)] to quench the trypsin and centrifugation at 220 g, 4 min, 4°C. Samples were resuspended in 25mL staining media, filtered through 40 μm cell strainer (Falcon), overlaid onto 10mL chilled Opti 1.1 solusion [to prepare Opti1.1 solution: First, 60% Optiprep (Sigma) was diluted in H$_2$O to 40%, and then further diluted with HBSS at a ratio of 2:3] and centrifuged at 800 g for 20 min, 4°C, using low acceleration and low brake. Following separation, cells were transferred to new 50mL Falcon tube, centrifuged at 220 g, 4 min, 4°C. Cells were resuspended in Tu2% media and seeded in a 24 well plate. Cells were grown in Tu2% media for 5 passages, until all fibroblasts were removed. During passaging, cells were detached using Versen (Lonza).

Histology

For immunohistochemistry and immunofluorescence, tumors were excised at days 10-15 post inoculation as indicated, fixed in 2.5% (w/v) paraformaldehyde for 24 hours and restored in 1% paraformaldehyde until embedded in paraffin for histological analysis. Immunohistochemistry for CD8a was performed on deparaffinized and rehydrated 4-μm thick paraffin-embedded sections. Endogenous horseradish peroxidase activity was blocked by H$_2$O$_2$ for 30 min. Antigen retrieval was performed with Tris-EDTA in a microwave oven for 25 min. For nonspecific binding, sections were blocked with 20% normal horse serum and 0.1% triton. Following blocking treatment, slides were incubated overnight at 4°C with primary antibody (a-CD8a rat monoclonal antibody, diluted 1:50, Clone 4SM15, eBioscience). Later, sections were incubated with biotinylated anti-rat secondary antibody (Biotin anti Rat IgG (H+L), CN- 712-065-153, Jackson ImmunoResearch) and exposed to a solution of 3- 3'-diamino-benzidine tablets (Sigma), washed, and counterstained by hematoxylin (Sigma) and dehydrated. Stained sections were examined and photographed on a bright-field microscope (Eclipse Ni-U; Nikon) equipped with Plan Fluor objectives (10x; 20x; 40x; 60x) connected to a CCD camera (DS-Fi2, Nikon). For Histology quantification, stained slides were counted manually by counting the number of positive CD8a cells per four-high-power fields, randomly chosen, from the margin of the tumor versus the tumor core. Immunofluorescence stainings for CD3$^+$ and FoxP3$^+$ cells were performed on 2-μm and 4-μm paraffin sections. Sections were incubated in acetone for 7 min at -20°C and antigens were retrieved in Tris-EDTA in a microwave oven for 10 min. Additionally, for nonspecific binding sections were blocked with 20% normal horse serum and 0.1% triton for 90 min in a humidity chamber. Following blocking, treatment slides were incubated overnight at 4°C with primary antibodies [(anti-CD3$^+$ rabbit monoclonal antibody [SP7] diluted 1:25, ab16669, ABCAM) and anti-FoxP3 rat monoclonal antibody (FJK-16 s) diluted 1:25, CN-14-5773-82, eBioscience]. Slides were then incubated with secondary

antibodies (Cy2 conjugated anti-rabbit, CN- 711-225-152; and Cy3 conjugated anti-rat, CN- 712-165-153, respectively; both antibodies from Jackson ImmunoResearch). Sections were counterstained by Hoechst (Invitrogen). Stained sections were examined and photographed with a fluorescence microscope (Eclipse Ni-U; Nikon) equipped with Plan Fluor objectives (10x; 20x; 40x; 60x) connected to a color camera (DS-Ri1, Nikon) microscope. Images were analyzed using FIJI ImageJ software.

CPD detection
Non-irradiated and UVB irradiated (600J/m2) B2905 cells were subjected to immunoflorescence stain; immediately following irradiation, cells were fixed with 2.5% PFA in order to prevent any CPD repair, washed, and treated with 2N HCL for DNA denaturation, followed by re-equilibration with 0.1M Borate buffer, PH 8.5. CPD were detected via anti-CPD antibody (NMDND001, Cosmo Bio, 1:400), followed by anti-mouse Cy3 stain (Cy3 conjugated anti-mouse,715-165-151, Jackson ImmunoResearch). Stained cells were examined and photographed with a fluorescence microscope (Eclipse Ni-U; Nikon) equipped with Plan Fluor objectives (10x; 20x; 40x; 60x) connected to a color camera (DS-Ri1, Nikon) microscope.

DNA-Sequencing and analysis
Genomic DNA was extracted from cell lines using the QIAGENe DNeasy Blood & Tissue Kit. Exome capture was performed using the SureSelectXT Mouse All Exon System (Agilent Technologies, Wilmington, DE USA, catalog# 5190-4641). Mapping and variant analysis reads were mapped to the mouse genome (GRCm38, mm10) using BWA (Li and Durbin, 2010) with default parameters. On average, we generated a mean depth of $100 \times$ to achieve exome builds with at least 90% of the exomes covered by high quality genotype calls. The Picard MarkDuplicates module was used to remove the duplicates from the data. The Genome Analysis Tool Kit (GATK-Lite) toolkit (v2.3) (McKenna et al., 2010) module IndelRealigner and BaseRecalibrator were used to preprocess the alignments. The Picard MarkDuplicates module was used to remove the duplicates from the data. The Genome Analysis Tool Kit (GATK-Lite) toolkit (v2.3) module IndelRealigner and BaseRecalibrator were used to preprocess the alignments and variant analysis. During base quality recalibration, dbSNP variants were used as known sites, according to GATK Best Practices (DePristo et al., 2011). Target-capture efficiency metrics were determined using Target region coverage calculator Version 0.0.1. The realigned and recalibrated BAM file was used as an input to UnifiedGenotyper module from the GATK-lite toolkit (v2.3). During base quality recalibration. Sorting and indexing were performed using samtools v1.8 (Li et al., 2009). Variant calls were restricted to the target regions (Agilent SureSelectXT Mouse All Exon). Polymorphisms were removed by examination of the sequencein genomic DNA from matched normal tissue (kidney). For further confidence, mouse SNP filtration was applied to the VCF files based on normal mouse spleen SNPs. Finally, somatic-mutations associated with less than 10 reads were filtered-out.

Cancer Signature analysis
Called exonic mutations and the tri-nucleotide 96 mutations context were counted to assess the genomic effect of UVB treatment in the mutational landscape of the cell lines. Deconstructsig R package was applied to obtain the signatures (*ref in https://www.ncbi.nlm.nih.gov/pmc/articles/PMC4762164/)

Genetic heterogeneity analysis of melanoma cell lines
VCF files were converted to MAF files (v2.4) using vcf2maf. To evaluate the genetic heterogeneity of the cell lines, we look at the variant allele frequency (VAF) of the exonic mutations (Missense, silent, nonstop, and nonsense mutations, and in-frame insertion, frameshift insertion, on-frame deletion, and frameshift deletion) and defined mutations with a VAF > 0.25 as more likely to be clonal mutations and vice versa, as previously defined (Williams et al., 2016). Two-sided Mann-Whitney test with continuity correction, Fisher's exact test, and two-sided Smirnov-Kolmogorov test were used to compared the VAF distributions between parental control and parental + UVB cell lines. All tests produced the same result.

Production and purification of membrane MHC molecules
B2905 cell pellets were collected from $2x10^8$ cells, lysed with cold lysis buffer [containing 0.25% sodium deoxycholate (Sigma), 0.2mM iodoacetamide (Sigma), 1mM EDTA (Promega), 1:300 Protease Inhibitors Cocktail (Sigma), 1mM PMSF (Sigma) and 1% octyl-β-D glucopyranoside (Sigma) in PBS] for 1 hour with gentle rotation, at 4°C. Lysates were centrifuged at 48,000 g for 60 minutes at 4°C, and then were passed through a pre-clearing column containing Protein-A Resin (A2S). MHC molecules and their bound peptides were immunoaffinity purified using the 20-8-4 and 28-14-8 antibodies against H2-Kb and H2-Db, respectively covalently bound to Protein-A Sepharose beads (Bassani-Sternberg et al., 2010; Milner et al., 2013). Affinity column was washed with 400mM NaCl, 20mM Tris–HCl followed by 20mM Tris–HCl, pH 8.0 washing steps. The MHC molecules and bound peptides were then eluted with 1% trifluoracetic acid followed by separation of the peptides from the proteins by binding the eluted fraction to disposable reversed-phase C18 columns (Harvard Apparatus). Elution of the peptides was done with 30% acetonitrile in 0.1% trifluoracetic acid (Milner et al., 2013). The eluted peptides were then cleaned using C18 stage tips as in (Rappsilber et al., 2003).

Identification of the MHC peptides

The MHC peptides were dried by vacuum centrifugation, re-solubilized with 0.1% Formic acid and resolved on capillary reversed phase chromatography on 0.075x200 mm laser-pulled capillaries, self-packed with 3μ Reprosil-Aqua C_{18} (Ishihama et al., 2002). Electrospray tandem mass spectrometry was performed with the Q-Exactive-Plus mass spectrometer (Thermo Scientific).

To construct the database used for peptidomics analysis, non-synonymous somatic point-mutations obtained from WES data, were used to generate a list of mutated peptides. A sliding-window approach of 9-11 amino acids in length was used, to obtain the mutated amino acid in all possible positions. The binding affinity of every mutant peptide was predicted using netMHC-4.0 (Nielsen et al., 2003). Subsequently, only neoantigens with a predicted binding affinity of < 500 nM were extracted, similar to previous studies (McGranahan et al., 2016). The MS data was analyzed by MaxQuant (Cox and Mann, 2008) version 1.5.3.8. The MS files were run against the predicted neoantigen database, in combination with the full WT mouse proteome obtained from f the Uniprot database (http://www.uniprot.org) from Apr-2017 (70946 entries).

In addition, targeted proteomics was used for the identification of neoantigens. In this case the MS instrument measures a predefined list of masses (peptides), also known as Parallel Reaction Monitoring (Lesur and Domon, 2015; Shi et al., 2016). The experiment included analysis of synthetic peptides (GenScript), which were identical in their sequence to the native peptides.

The spectra of the synthetic peptides (MaxQuant) of all identified neopeptides was compared to that of the neoantigenes identified (https://github.com/bioinf-dev/Wolf_et_al_Cell_2019/blob/master/Other/Spectra.pdf) for confirming the identity of the neoantigenes. All neopeptides identified by this targeted approach are indicated in Table S3.

Hydrophobicity calculation

Average hydrophobicity of predicted neoantigens was calculated using R software ("Peptides" library, "KyteDoolittle" scale). A bias toward hydrophobic amino acids at T cell receptor contact residues within immunogenic peptides was previously identified (Chowell et al., 2015).

RMA-S peptide binding assay

RMA-S cells were cultured until logarithmic phase. Cells were washed twice in PBS and incubated in serum-free RPMI medium for 90 minutes in 37°C. Following incubation, $2*10^5$ cells/well were incubated with 0.1-100 μM peptide in 37°C. 18 hours later, surface H2-Db and H2-Kb levels were assessed by FACS via APC anti-mouse H-2Kb and PE anti-mouse H-2Db antibodies (BioLegend), respectively. Analysis was done using FlowJo software (Tree Star). All peptides were purchased from GenScript.

Inference of ITH, mutation and CNV load

From the TCGA data access portal (https://portal.gdc.cancer.gov/), we downloaded level 2 SNP array and germline + somatic variant call data (*.byallele.copynumber.data.txt, *.oxoG.snp.capture.tcga.vcf.) for 432 skin cutaneous melanoma tumor and matched normal samples. Across all 432 patients, we apply CHAT (Snyder et al., 2014) under default package settings to estimate tumor purity followed by estimation of cellular abundance of CNVs and somatic mutations from the SNP array and variant call data respectively. We found that the average sample purity estimated by CHAT is ~74% with only 14 samples having purity less than 25%. However, we do not pre-filter any of these samples in our downstream survival analyses as our final conclusions remain the same even after their removal. To estimate mutation load per sample, we count the number of somatic variant calls that were classified as missense or nonsense per sample. This data was obtained from the cbioportal website (https://www.cbioportal.org). Since CHAT detects CNVs using the circular binary segmentation algorithm (Olshen et al., 2004), which essentially partitions the genome into non-overlapping sections of same copy number, we estimate CNV load per sample in a manner similar to Andor et al. (2016). To elaborate: for a tumor sample, let L_s be the length of a segment s of the genome and let CN_s be total copy number of that segment inferred by CHAT while considering the tumor purity. Let $X_s \in \{0, 1\}$ be an indicator of deviation of CN_s from normal diploid copy number of 2. Then, CNV load is defined as:

$$\text{CNV load} = \frac{\sum_{s:X_s=1} L_s}{\sum_s L_s}$$

Given that tumor evolution is characterized by a series of clonal expansion events, we often find that mutations and CNVs detected from a bulk tumor sample group into clusters. The number of these clusters *or clones* is interpreted as the intra-tumor heterogeneity. Using CHAT, we can derive two estimates of number of clones by – clustering cellular abundances of somatic mutations (ITH1) or clustering cellular abundances of CNVs (ITH2). Both estimates convey important information of the underlying clonal structure at different resolutions. Hence, we set the overall intra-tumor heterogeneity of a sample as:

$$\text{ITH} = \max(\text{ITH1, ITH2})$$

Given the limitation of a single bulk tumor sample per patient for inference, the above estimate is a lower bound and correlated with tumor purity (spearman's rho = 0.232, p value = 2.09E-5). However, we show that our downstream results still hold after correcting for tumor purity, age and stage (see below).

TCGA Survival Analysis

To see if mutation load, CNV load and ITH are associated with overall patient survival, we stratified the TCGA patients into the following groups:

- Low mutation load ($\leq$median), high mutation load (> median)
- Low cnv load ($\leq$median), high cnv load (> median)
- Low ITH ($\leq$median), High ITH (> median)

Given a cohort of 402 patients with available clinical data, we then fit Kaplan-Meier survival curves for each group and their combinations and test if there are any significant survival differences between the groups using a Log-rank test. All survival analyses were performed using the survival package readily available for R. Due to potentially confounding effects of purity and other clinical factors, it is necessary to ascertain whether the observed associations with survival still hold after accounting for confounding factors. The three major potentially confounding factors are tumor purity, patient age and clinical stage. We hence performed a multivariate cox regression analysis in which patient age, tumor purity and clinical stage were included as additional factors. Our original conclusions do not change after running this analysis (See Table S6).

Estimating cytolytic activity from RNA-seq data

Single-end RNA Seq data from the mouse cell-line derived tumors was trimmed using Trimomatic (0.36) to filter out low quality and adaptor reads. The trimmed data was then processed using Salmon (0.9.2) to directly quantify gene expression levels (TPM). Furthermore, gene expression levels (RPKM) of the 330 melanoma patients with corresponding survival information were downloaded from the TCGA portal. Cytolytic activity (CYT) of TILs in the mouse cell-line derived tumors, and likewise in patient tumors, was estimated from the geometric mean of expression levels of GZMA and PRF1[13].

$$CYT = \exp\left(\frac{\ln(GZMA + 1) + \ln(PRF1 + 1)}{2}\right)$$

Phylogenetic analysis of mouse UVB and SCCs

Exome sequencing data for the UVB exposed sample (n = 1) and the individual single cell clones (n = 20), were used for joint clustering to infer the subclones present across this combined set of samples. MAF files (generated as described above) and somatic copy number alteration logR scores by segment (generated using CNVkit), were utilized as input to the SciClone clustering algorithm (Miller et al., 2014). To ensure high confidence clonal markers were used, the following variant filters were applied: i) a minimum alternative read depth of > 5 was used, ii) indels and triallelic sites were excluded, and iii) only variants present in $\geq$ 2 samples were retained (i.e., private mutations only in one sample were excluded). This latter criteria of filtering out private variants was implemented to minimize the impact of technical artifacts, which are known to be a potential issue in ITH analyses (Shi et al., 2018), as well as the fact that variants found only in one sample offered minimal utility in inferring the overall cross-sample phylogeny. For completeness, the proportion of private variants found in the experimental mixes used in Figure 6 is included in Table S7, and further studies with high depth error corrected sequencing will be required to accurately understand the biological role of private mutations. SciClone was run with the following parameters: copyNumberMargins = 0.5, maximumClusters = 30 and minimumDepth = −1 (variants were already prefiltered for minimum depth of > 5 alternative reads during MAF file creation). The clustering solution from SciClone was manually reviewed, and any obviously poor quality clusters were removed (e.g., clusters defined by < 10 mutations, clusters present in every sample but with low VAF values (< 25%), duplicated clusters). Phylogenetic trees, and representative sample tumor diagrams were constructed using R package CloneEvol (Dang et al., 2017). Individual single cell clones were mapped to terminal clones/branches (from the overall clustering solution), based on the closest fitting VAF frequency.

Shannon diversity index analysis

Four malignant melanoma cohorts were analyzed, from previously published studies by Snyder et al. (anti-CTLA4 treated), Riaz et al. (anti-PD1 treated), Hugo et al. (anti-PD1 treated) and Van Allen et al. (anti-CTLA4 treated). Pyclone clustering results for the Riaz et al. cohort were obtained directly from the authors supplemental data files (https://github.com/riazn/bms038_analysis/tree/master/data), and clones defined by n $\geq$ 2 mutation were retained for further analysis. Pyclone clustering results for the Snyder et al. (2014) and Van Allen et al. (2015) cohorts were obtained from previously published work from McGranahan et al. (2016) (https://bitbucket.org/nmcgranahan/clonalneoantigenanalysispipeline/downloads/), with clones already having undergone quality control filtering. For Hugo et al. (2016), no previously published clustering results were available, and instead we managed to successfully process raw WES data of a subset of 22 samples for which there is available survival information on 21 samples. The processing pipeline used is as follows: we called variants for each cancer and paired normal samples using the GATK (V. 3.6) 'HaplotypeCaller'(Li et al., 2009; McKenna et al., 2010) utility applying '-ERC GVCF' mode to produce a comprehensive record of genotype likelihoods for every position in the genome regardless of whether a variant was detected at that site or not. The goal of using the GVCF mode was to capture confidence score for every site represented in a paired normal and cancer cohort for calling somatic mutation in cancer. Next, we combined the paired GVCFs from each paired cohorts using GATK's 'GenotypeGVCFs' utility

yielding genotype likelihood scores for every variant in cancer and the paired normal sample. Next, we used GATK's 'VariantRecalibrator' utility using dbSNP VCF (v146: ftp://ftp.ncbi.nlm.nih.gov/snp/organisms/human_9606_b146_GRCh38p2/VCF) file by selecting annotation criteria of QD;MQ;MQRankSum;ReadPosRankSum;FS;SOR, followed by GATK's 'ApplyRecalibration' utility with 'SNP' mode. Next, using GATK's 'VariantFiltration' utility we selected the variants with VQSLOD $\geq$ 4.0. Finally, somatic mutations were defined as the loci whose genotype (1/1, 0/1, or 0/0 with 'PL' (Phred-scaled likelihood of the genotype) score = 0, i.e., highest confidence) in cancer is distinct from that in paired normal. The final somatic mutations were mapped on an exonic site of a transcript by 'bcftools' tool (V. 1.3)(Li et al., 2009) using BED file of coding region. Clustering analysis was then completed using the CHAT algorithm, as described above.

For each case, the count of mutations within each cluster (clone) as defined by Pyclone/CHAT were computed, and Shannon diversity index (SDI) was calculated using the entropy.empirical function in R package 'Entropy'. Overall survival data was obtained from the original author's publications, and n = 3 cases from the Riaz et al. cohort with "NE" RECIST coding were excluded, on account of death having occurred prior to disease assessment. In addition, the group of n = 10 cases from the Van Allen et al. (2015) cohort with long-term survival but no clinical benefit from anti-CTLA4 treatment were excluded, as per the original publication. All other cases with available survival data and clustering results were used for survival analysis (cases with available clustering results were those with data deposited in https://github.com/riazn/bms038_analysis/tree/master/data (Riaz et al., 2017) and https://bitbucket.org/nmcgranahan/clonalneoantigenanalysispipeline/downloads/ (Van Allen et al., 2015 and Snyder et al., 2014 cohorts), extracted on date 14/05/2019, please refer to the original publications for further details). Kaplan-Meier plots were drawn using the ggsurvplot function in R, with the low/high diversity groups being defined by having a SDI value < or $\geq$ to the median value in each cohort respectively. Significance values in Figure 7 were calculated using the coxph function in R, with SDI included in the model as a continuous variable, and overall survival hazard ratios are reported per unit increase in SDI score. To correct for purity, a multi-variable coxph model was used, with SDI and purity included as variables, and the significance values of each variable in the model were analyzed. Meta-analysis of significance across the two studies was calculated using the Fisher method for combinig p values.

QUANTIFICATION AND STATISTICAL ANALYSIS

Statistical analysis was performed using the Prism 8 software (GraphPad, San Diego, CA, USA) and the software environment R, using RStudio. For all statistical analysis a p value of < 0.05 was determined to be significant. All data is presented using standard error mean (SEM). P values are depicted in all figures, and selected p values with exceptional significance to the paper are also briefly described in the main text. Samples sizes (n), means and SEM are depicted in the figures and/or figure legends. Sample size values were either depiction of number of mice used for experiments, or number of patients. For the comparison of patient survival curves (Kaplan-Meier curves) the log rank test was used. For samples with distribution other than normal, or with small sample size (n < 6), the nonparametric Wilcoxon test, Mann-Whitney's U test, and Kruskal-Wallis test were used. For samples which approximate normal distribution, Student's t test or one-way ANOVA followed by Bonferoni's post hoc test was used. For correlation between CYT score and the ITH ranks depicted in Figure 1, the Spearman's Rho nonparametric test was used. For tumor growth curve, repeated-measures two-way ANOVA was used, followed by Bonferoni's post hoc test. For the analysis of the Shannon diversity index (SDI), z-test from Cox proportional hazard mode was used with SDI tested as a continuous variable. Proportions of genomic mutation types of the different cell lines were analyzed using the Chi-Square test.

DATA AND CODE AVAILABILITY

The raw sequencing data has been made publicly deposited at https://www.ebi.ac.uk/ena. The study accession number is PRJEB25961 and the secondary accession is ERP107928. The custom codes and processed data used to generate the results of the manuscript (Mouse CD8+ T cell RNaseq data, Processed data and code used; Figures 1, 2, 3, and 7 and the peptydes ms spectra) are available in github (https://github.com/bioinf-dev/Wolf_et_al_Cell_2019)
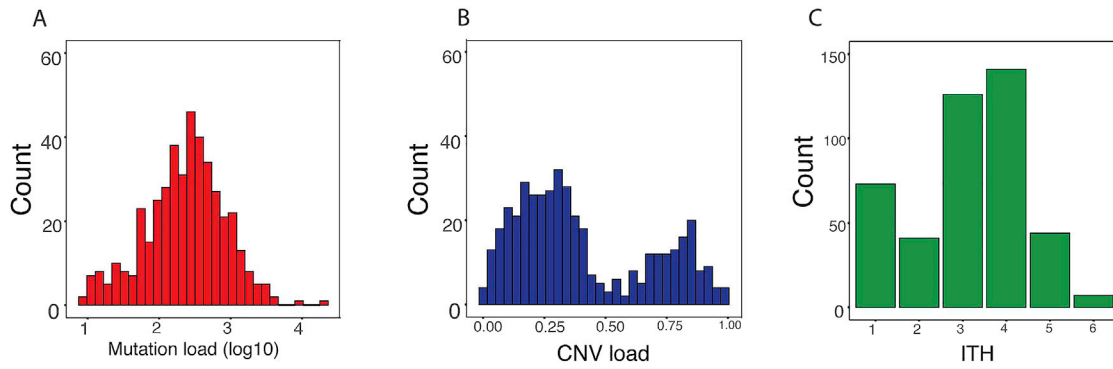
Figure S1. Characteristics of Human Melanoma TCGA Data, Related to Figure 1

A) Distribution of the somatic mutation load (silent + non-silent) on a log10 scale. B) Distribution of CNV load – defined as fraction of the genome affected by CNV.
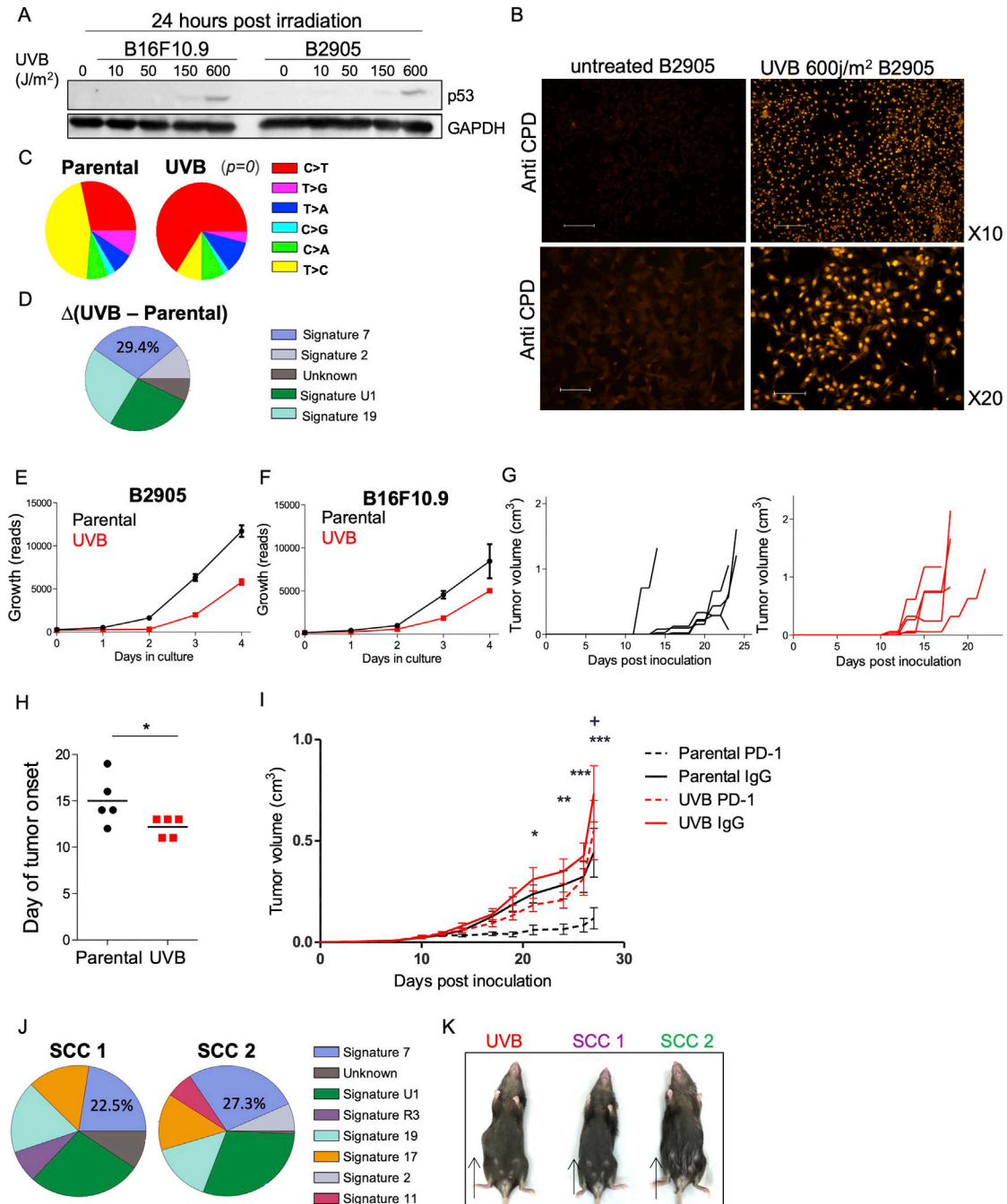C) Distribution of the overall intra tumor heterogeneity estimated using CHAT (See STAR Methods).

Figure S2. *In Vitro* and *In Vivo* **Assessment of UVB-Treated Cells, Related to** Figure 2 **and** Table S2

A) western blot for p53 and GAPDH in B16F10.9 and B2905 cells 24h post irradiation in various UVB dosages. B) Immunofluorescence stains for UVB-induced cyclobutane pyrimidine dimer (CPD) in parental B2905 cells -untreated (left) and UVB irradiated (right). The UVB irradiated cells were fixed, washed and subjected to immunostaining two minutes after irradiation. Scale bar represents 200 μM (for 10x magnification) and 100 μM (for 20x magnification). C) Distribution of somatic alterations in the parental cell line, in comparison to those occurring following UVB exposure show increase in C > T alterations (distribution of added mutations is shown relative to parental). p value was calculated based on the Chi-square test D) Mutation signatures identified by DeconstructSigs for the mutation changes following UVB irradiation (UVB B2905 versus Parental cell line). E-F) *In vitro* proliferation of parental versus UVB irradiated B2905, and B16F10.9, respectively, starting from 500 cells at day 0. Data are mean ± SEM. G) *In vivo* tumor growth in mice inoculated with parental B16F10.9 (left panel) and UVB irradiated B16F10.9 (right panel). n = 5, data are representative of two independent experiments. H) Day of tumor onset for the experiment shown in G. I) *In vivo* tumor growth in mice inoculated with parental B2905 (Black) or UVB irradiated B2905 (red) lines, treated with anti-PD-1 or IgG control antibodies at days 6, 9, and 12 post cells

inoculation (n = 11-12). Data are mean ± SEM. Comparisons between parental B2905 tumors treated with IgG or anti-PD-1 treated are depicted by asterisks, whereas comprisons between UVB B2905 tumors treated with IgG or anti-PD-1 are depcited by cross. *,+p < 0.05, **p < 0.01, ***p < 0.001, one-way ANOVA followed by Tukey's post hoc test, J) Mutation signature 7, associated with UVB exposure, is identified in SCC 1 and 2 (deconstructSigs tool). K) Macroscopic tumor growth for tumors derived from UVB, SCC 1 and SCC 2 at day 15.

(legend on next page)
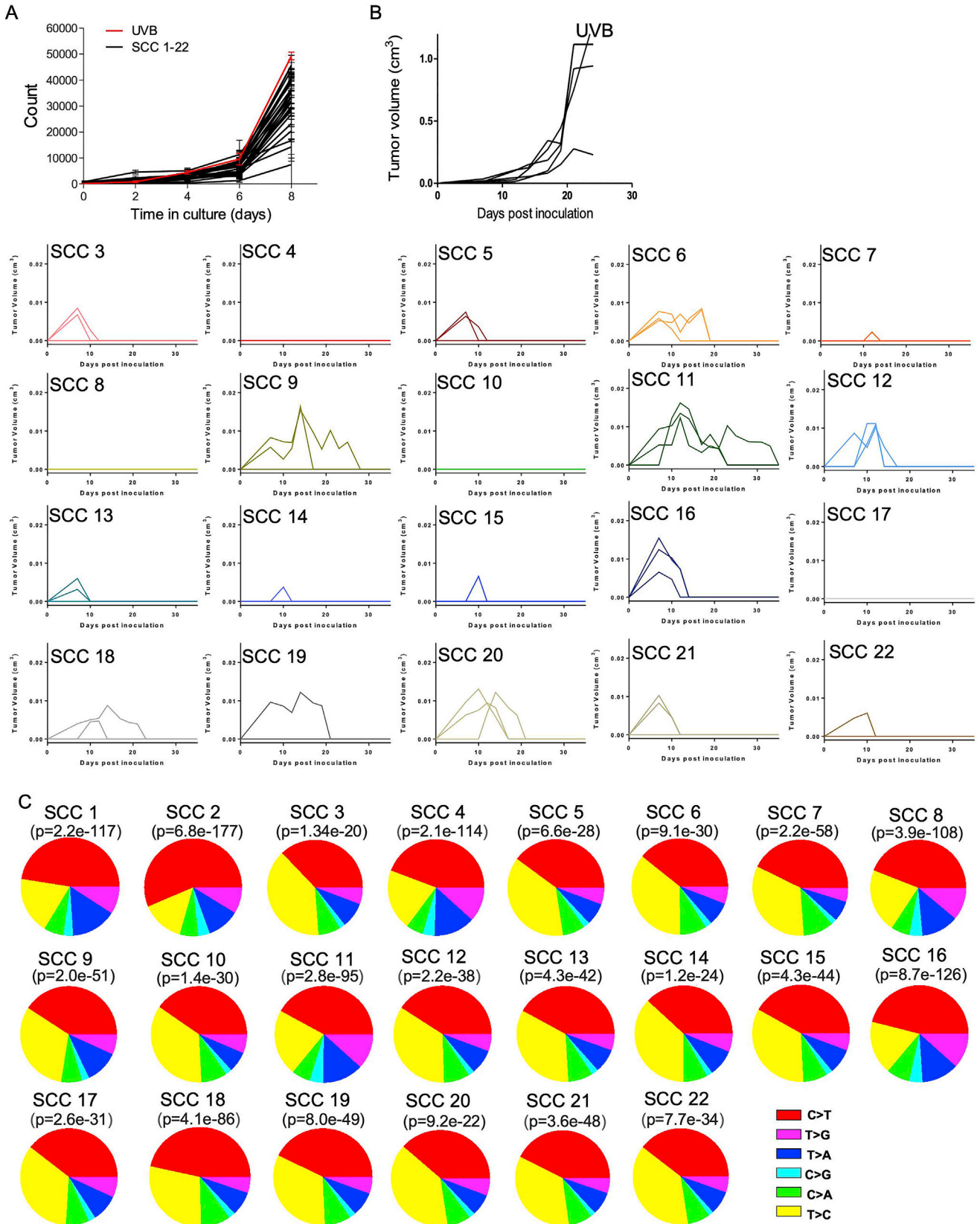
Figure S3. Supplemental Data for SCC 1–22, Related to Figure 3

A) *In vitro* growth of UVB irradiated B2905, and the 22 single cell clones derived from it, measured by SyberGreen proliferation assay. Data are mean ± SD. B) *In vivo* growth of the UVB irradiated B2905 cells and all 20 SCC depicted in Figure 3A, presented individually. n = 3 for each single cell line inoculation. n = 5 for the UVB irradiated B2905 line. C) Somatic alteration distributions of all SCCs show significant difference in comparison to the parental cell line (mutations added relative to parental are shown) p value was calculated based on the Chi-square test.
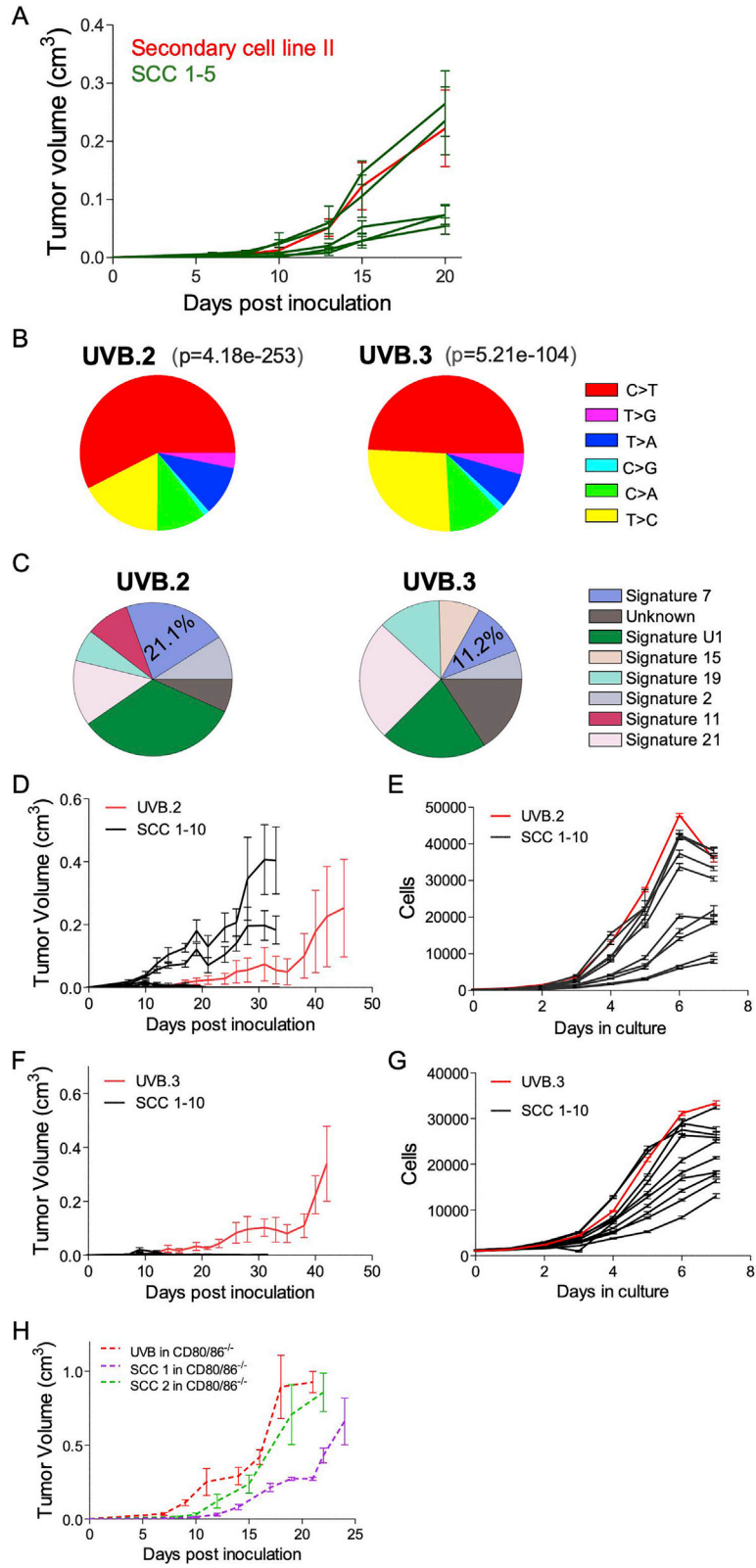
A

B

UVB.2 (p=4.18e-253)   **UVB.3** (p=5.21e-104)

- C>T
- T>G
- T>A
- C>G
- C>A
- T>C

C

UVB.2   **UVB.3**

21.1%   11.2%

- Signature 7
- Unknown
- Signature U1
- Signature 15
- Signature 19
- Signature 2
- Signature 11
- Signature 21

D   E

F   G

H

Figure S4. Characterization of Additional UVB-Irradiated B2905 Lines and SCCs Derived from Them, Related to Figure 3

A) *In vivo* tumor growth in mice inoculated with a secondary cell line, derived from a UVB irradiated B2905 tumor (red, n = 5) or with 5 different SCC derived from this line. (green, n = 5). Data are mean ± SEM. B-G: Additional, independent, UVB irradiated B2905 cell lines: B) C > T somatic alterations are significantly most dominant following UVB exposure (mutations added relative to parental are shown). p value was calculated based on the Chi-square test. C) Signature 7 mutations associated with UVB exposure is obtained in UVB.2 and UVB.3 using deconstructSigs tool. D) *In vivo* tumor growth in mice inoculated with a UVB irradiated B2905 cell line, "UVB.2," (red, n = 6) or with 10 different single cell clones derived from this line. (black, n = 5). Data are mean ± SEM. E) *In vitro* growth of the cell lines described in D, measured using SyberGreen proliferation assay. Data are mean ± SEM. F) *In vivo* tumor growth in mice inoculated with a UVB irradiated B2905 cell line, "UVB.3," (red, n = 5) or with 10 different single cell clones derived from this line. (black, n = 5). Data are mean ± SEM. G) *In vitro* growth of the cell lines described in F, measured using SyberGreen proliferation assay. Data are mean ± SEM. H) *In vivo* growth of tumors derived from (the first) UVB irradiated B2905, SCC 1, and SCC 2 in CD80/86$^{-/-}$ mice. n = 4-7. Data are mean ± SEM.
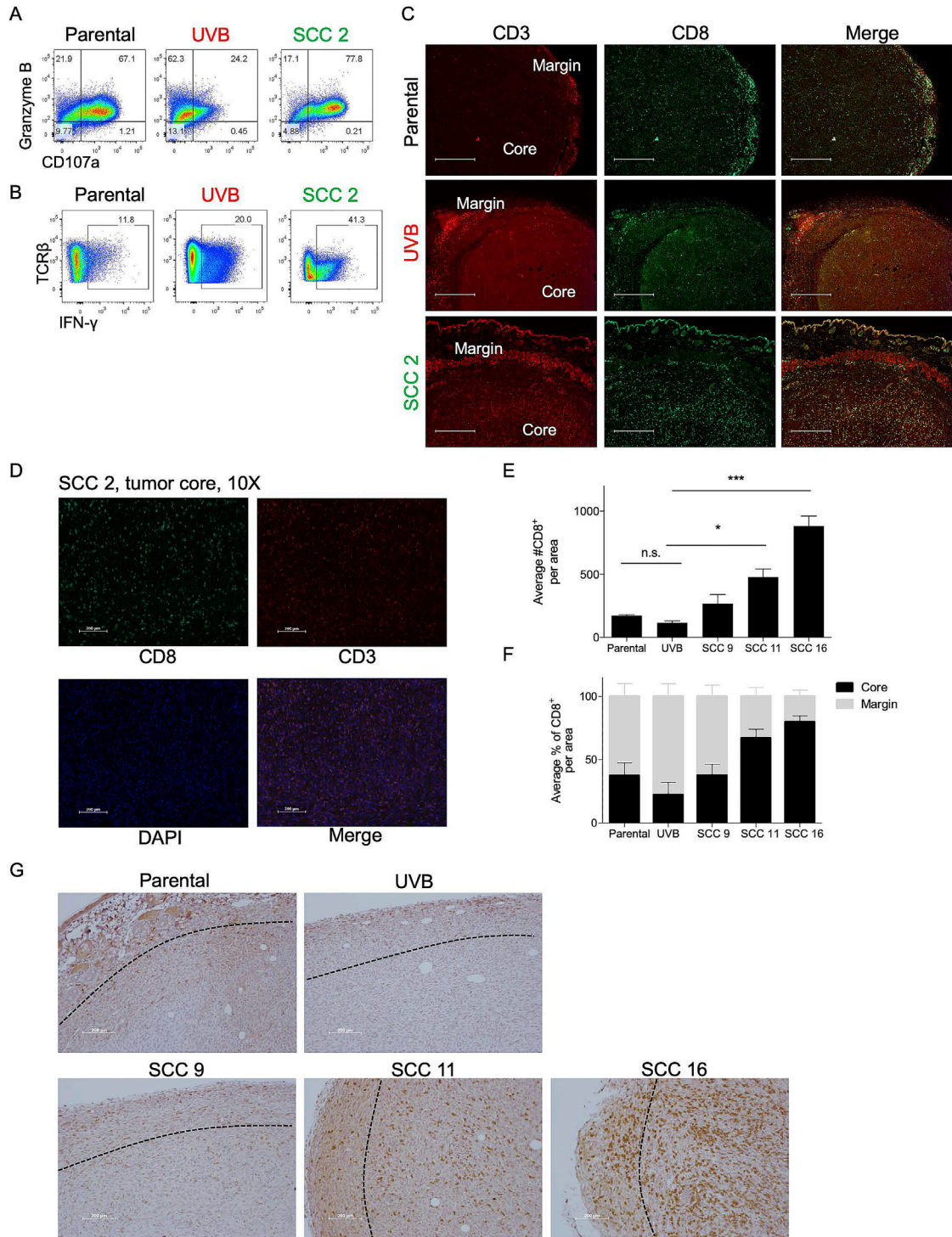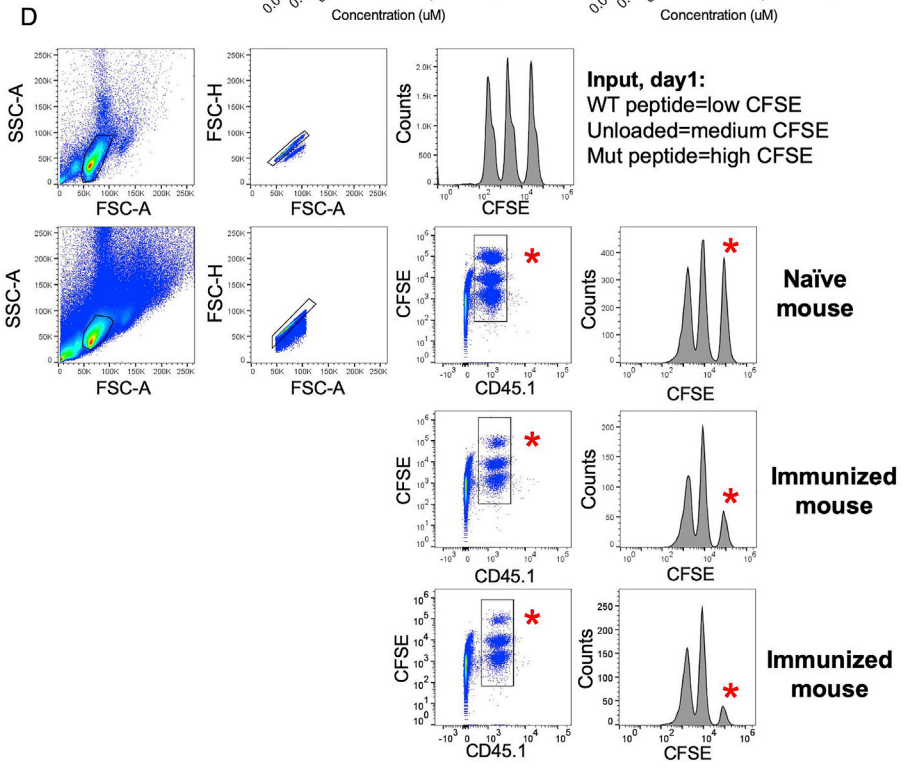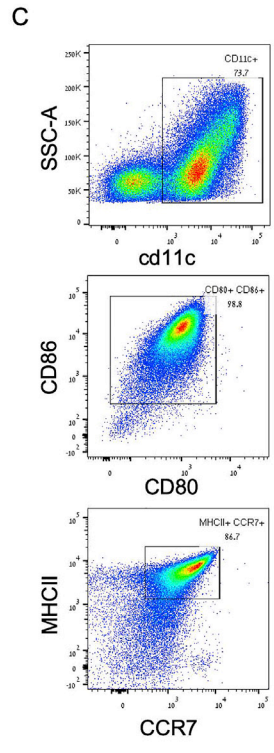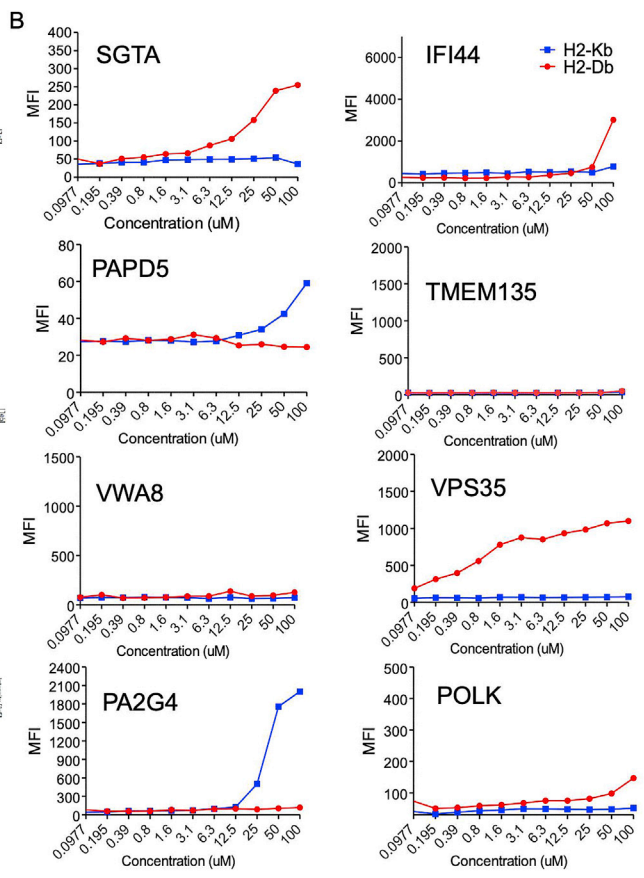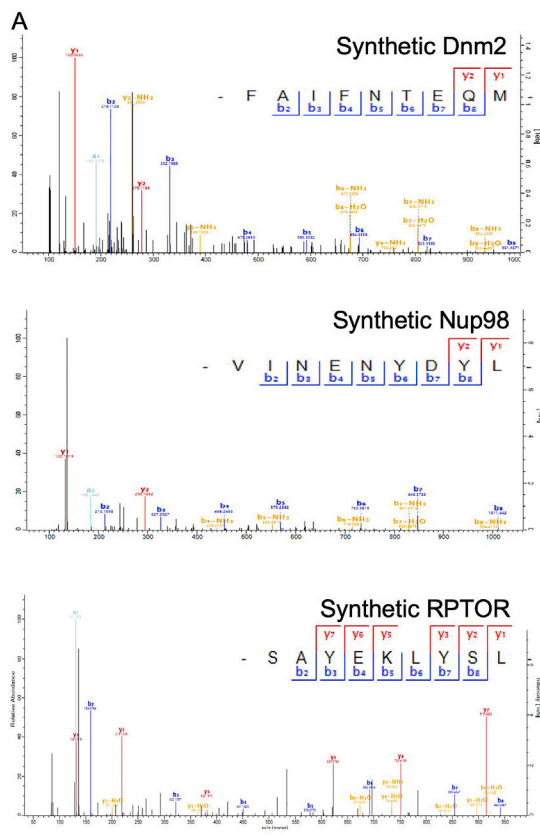
Figure S5. Differential TIL Activation and Infiltration in Differentially Heterogeneous Tumors, Related to Figure 4

A-B) Flow cytometry results of the analyses described in Figure 4 A-B. C) Immunofluorescence of CD3 and CD8 in slides taken from tumors derived by B2905 Parental, UVB and SCC 2. Magnification is 4X. Pictures are representative of three mice per group. Scale bar represents 500 μM. D) higher magnification (10X) of the SCC 2 core. Scale bar represents 200 μM. E-F) Quantification of CD8^{+} TILs infiltration (E, *p < 0.05, ***p < 0.001, One-way ANNOVA followed by Tuckey's post hoc test) and their core versus margin localization in tumors derived from B2905-parental, UVB, and SCC 9,11,16, at day 15 post inoculation. Significant differences are seen between UVB and SSC 11/16 but not between UVB and parental cell lines. n = 3-4. G) Representative immunohistochemical stain for CD8^{+} cells. Slides were taken from the tumors indicated above, at day 15 post inoculation. Scale bar represents 200 μM.

A

Synthetic Dnm2

- F A I F N T E Q M

Synthetic Nup98

- V I N E N Y D Y L

Synthetic RPTOR

- S A Y E K L Y S L

B

SGTA

IFI44

■ H2-Kb
● H2-Db

PAPD5

TMEM135

VWA8

VPS35

PA2G4

POLK

C

D

Input, day1:
WT peptide=low CFSE
Unloaded=medium CFSE
Mut peptide=high CFSE

Naïve mouse

Immunized mouse

Immunized mouse

(legend on next page)

Figure S6. Characterization of the Identified Neoantigens, Related to Figure 5

A) Mass spectra of synthetic peptides, identical in their sequence to the indicated neoantigens described in Figure 5. B) Differential binding of the identified neopeptides MHCI; Peptide binding to MHCI molecules was assessed via MHCI stabilization assay using RMA-S cells, incubated with the peptides at 0.1-100 μM for 18 hours. Surface expression of H2-D$_b$ and H2-K$_b$ was measured by flow cytometry. C) Flow cytometry analysis showing the BM-derived DCs after 10 days of maturation in culture. These cells were used for peptide vaccination. Results are representative of the three rounds of DCs vaccination. D) Flow cytometry analysis from day 1 (first row) and day 2 (rows 2-4) of the *in vivo* killing assay for the immunized versus naive mice. At day 1, Splenocytes from a CD45.1+ donor mouse were either loaded with wild-type peptide, unloaded, or loaded with a mutant peptide, labeled with CFSE low, medium and high concentrations, respectively, and subjected to flow cytometry analysis to assure these cells are in 1:1:1 ratios. This splenocytes mixture was injected either to naive mouse, or to 2-3 immunized mice (all CD45.2+). 24 hours later, the immunized mice splenocytes were subjected to flow cytometry analysis. The CD45.1$^+$CFSE$^+$ population was gated, and specific killing percentages were calculated, relative to the naive mice. The red asterisks point to the mutant peptide loaded cells at day 2, in the naive versus immunized mice. The above analysis, for noepeptide Dnm2, is a representative of the killing assays described in Figure 5, for three different neopeptides.
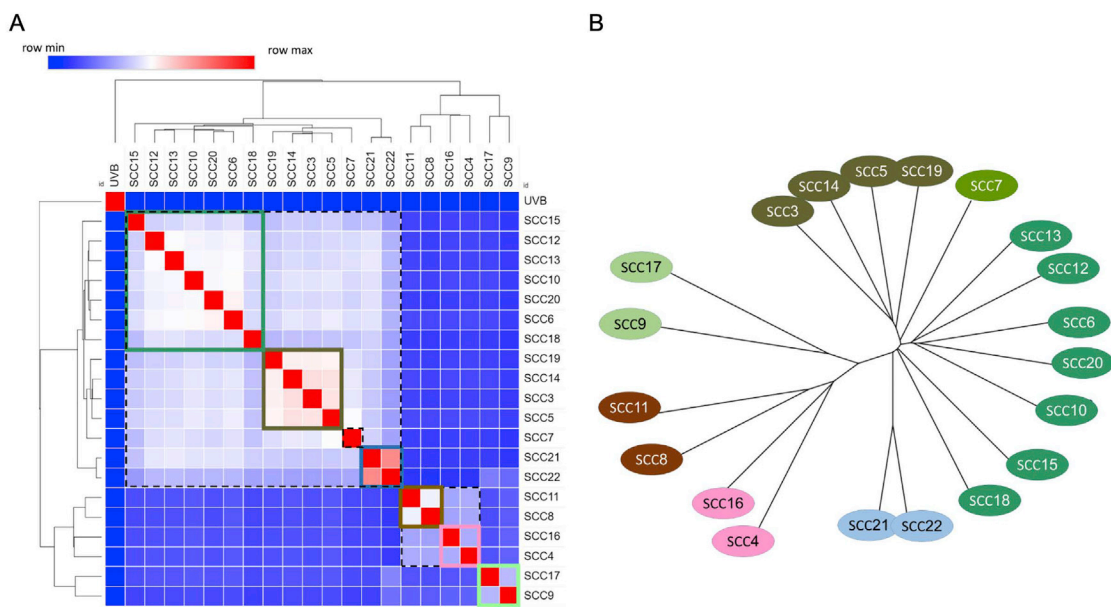
Figure S7. Single-Cell Clone Clustering of Shared Mutations and Phylogenetic Reconstruction, Related to Figure 6

A) Hierarchical Clustering analysis of correlations between SCCs, based on the fraction of shared mutations. B) Phylogenetic reconstruction of SCCs' mutations based on neighbor-joining tree estimation shows consistent results (phangorn R package).